Journal of Materials Science: Materials in Engineering

ORIGINAL PAPER

Open Access

Expounding the application of nano and micro silica as a complementary additive in metakaolin phosphate geopolymer for ceramic applications—micro and nanoscale structural investigation

N. Vanitha[1], Rithikaa Thanigaiselvan[1], M. Manivannan[1], R. Jeyalakshmi[1*], S. N. Megha[2] and M. Kesavan[3]

Abstract

Metakaolin phosphate geopolymers comprising poly-phospho-siloxo units are known for their structural performance, additionally advancing their microstructure with the transformation of crystalline berlinite phases at elevated temperatures. The intrinsic reaction of Al of metakaolin in the acid exploited, but the reaction of secondary silica phases is limitedly known. Metakaolin as a primary precursor (M) with the addition of 2% and 5% of nano silica (MS2 and MS5) and micro silica (MM2 and MM5) cast using 8-M phosphoric acid was cured at 80 °C. To enhance the utilization of geopolymer in any high-temperature applications, the structural transformations were studied after heating to various temperatures (200, 400, 600 and 800 °C) by XRD, Raman, TGA-DTA, SEM, XPS, FTIR and MAS-NMR. Sample M attained a strength of 46.2 MPa enhanced to 63.6 MPa in MS5 and 54.2 MPa in MM5. This can be ascribed from the transformation of Si–O–Al–O–Si into Si–O–Al–O–P from Raman bands. Comparing the chemical shift of Al (IV) to control, micro silica addition shifts the signal to a lower field (53 to 50 ppm) related to the increase of the number of Al-connected Si to give a tougher network. Nanoindentation is visualized from hardness and elasticity, and the corresponding values are 1.4 to 2.1 GPa and 0.8 to 1.4 GPa for loads ranging from 20 to 100 mN in silica-reinforced samples that are much higher than M. The micro and macro hardness is due to the reinforcement of quartz in micro silica around the gel. TGA-DTA showed that the reduction of mass loss is as high as 25.4% in control whereas 17.2% in MS5 and 15.8% in the MM5. Further, shrinkage rate in MS5 and MM5 was as low as − 1.1% and − 0.8% throughout the temperature range from 25 to 1000 °C and thus provides the way of use of nano and micro form of silica for better thermal resistance.

Keywords Metakaolin, Phosphate geopolymer, Micro silica, NMR, Raman, Shrinkage

*Correspondence:
R. Jeyalakshmi
jeyalakr@srmist.edu.in; rajyashree64@gmail.com
Full list of author information is available at the end of the article

Graphical Abstract

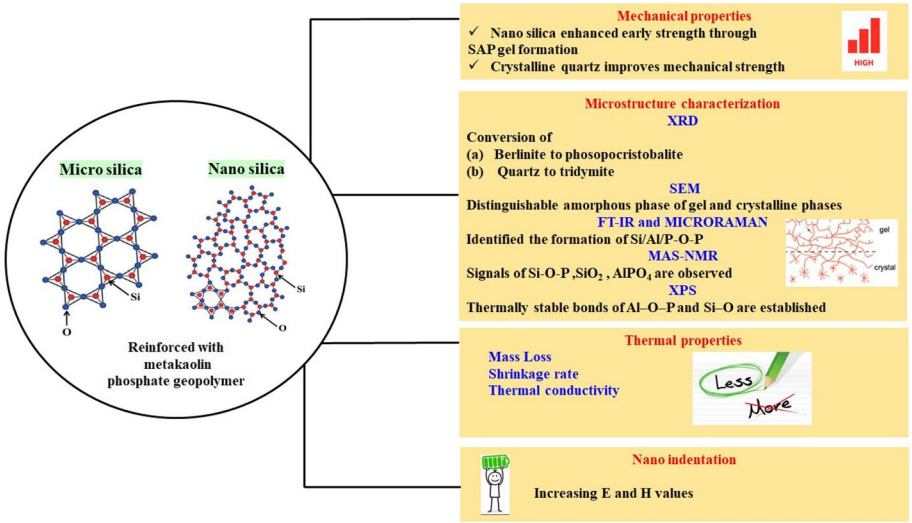

Introduction

Phospho-geopolymers or silico-aluminophosphate (SAP) cement is fabricated from aluminosilicate feedstock by the addition of phosphoric acid and cured at slightly elevated temperatures. The hardened geopolymers are composed of poly(phospho-siloxo) (Si–O–P–O–Si–O) units, 3D networks of [Si–O–P] and $AlPO_4$, which are connected by covalent bonds (Davidovits 2008; Cao et al. 2005). Unlike the sodium or potassium alumina silicate network in alkali-activated materials, the phospho-siloxo condensed product does not contain any network modifier (alkali cations). The reaction steps described in past research works are acceptable and prescribed mechanistic steps as dissolution of the aluminosilicate source materials in phosphoric acid, followed by the reaction of leached Al^{3+} ions with phosphate units to form the $AlPO_4$phase (Perera et al. 2008). The formation of Si–O–P bonds by partial replacement of Al by P, along with crystalline polymorphs of aluminium phosphate, has also been reported (Tchakouté and Rüscher 2017). The degree of reaction and the formed product slightly vary according to the reaction conditions.

Regarding the study of phosphate-based geopolymers under thermal treatment, the corresponding research studies are mostly restricted to metakaolin. Most of the thermal properties in the phospho-based network in lieu of alkaline ones are the thermal stability of aluminium phosphate, whereas alkali silicate melts at low temperatures owing to the presence of alkaline melting cations (Katsiki 2019; Wang et al. 2019; Zribi and Baklouti 2021). The most significant factor attributed to their exceptional thermal resistance is the phase changes of silico-aluminophosphate at different temperature regimes. The use of the acidic medium in the formation of macromolecular poly-siloxo chains is mainly described as SAP gel having Si–O–P–O–Al–Si networks (Khabbouchi et al. 2017). In addition to this, crystalline aluminium phosphate in berlinite forms is responsible for mechanical performance (Mathivet et al. 2019). Celerier et al. explained that phosphate-based geopolymers exhibit good thermal stability with no sign of melting up to the temperature of 1550 °C. Thus investigates the fire resistanceof the matrix at 1000 °C for 4 h with a heating/cooling rate of 5 °C/min whereas the matrix does not melt or is totally destroyed and proves the thermal stability of this kind of phosphate geopolymer matrix in such high temperature (Celerier et al. 2019; 2018). Our previous works on metakaolin-based phosphate networks focussed on the microstructural assessment before and after thermal treatment (Vanitha and Jeyalakshmi 2023).

Douiri et al. examined the dielectric and thermal performance of phosphoric acid metakaolin-based geopolymers as a function of the amount of H_3PO_4added to metakaolin. Thermal stability with no sign of melting up to 1550 °C was found (Douiri et al. 2014). Celerier et al. and M. Sellami et al. reported on the matrix's low dielectric nature in addition to its structural and thermal properties (Celerier et al. 2019; 2018; Sellami et al. 2019). Y. He et al. developed the matrix using Al_2O_3–$2SiO_2$powder hardened by curing at a slightly elevated temperature and studied the phase evolution upon heat treatment (He et al. 2016). Scanning throughout the literature, multiple

works focussed on the thermal behaviour of phosphate-based geopolymers were found, and a few important results are presented in Fig.1.

Some of the ongoing efforts to enhance the properties and performance of geopolymer cement involved in the variation of Si/Al, Al/P, curing temperature, method of curing, addition of active ingredients, etc. (Zribi et al. 2020). One of the best options is the integration of nano additives into these bulk geopolymers due to their excellent reactivity, enhancing physicochemical properties and suitability as reinforcement materials (Gowda et al. 2017; Heikal et al. 2015; Shaikh and Supit 2014; Senff et al. 2009). The addition of microscale reinforcements in the form of fibres or particles in the geopolymeric network has attracted the attention of material researchers because it has been shown to improve the toughness and strength and reduce crack width and shrinkage (Nochaiya et al. 2010). Among all the tested

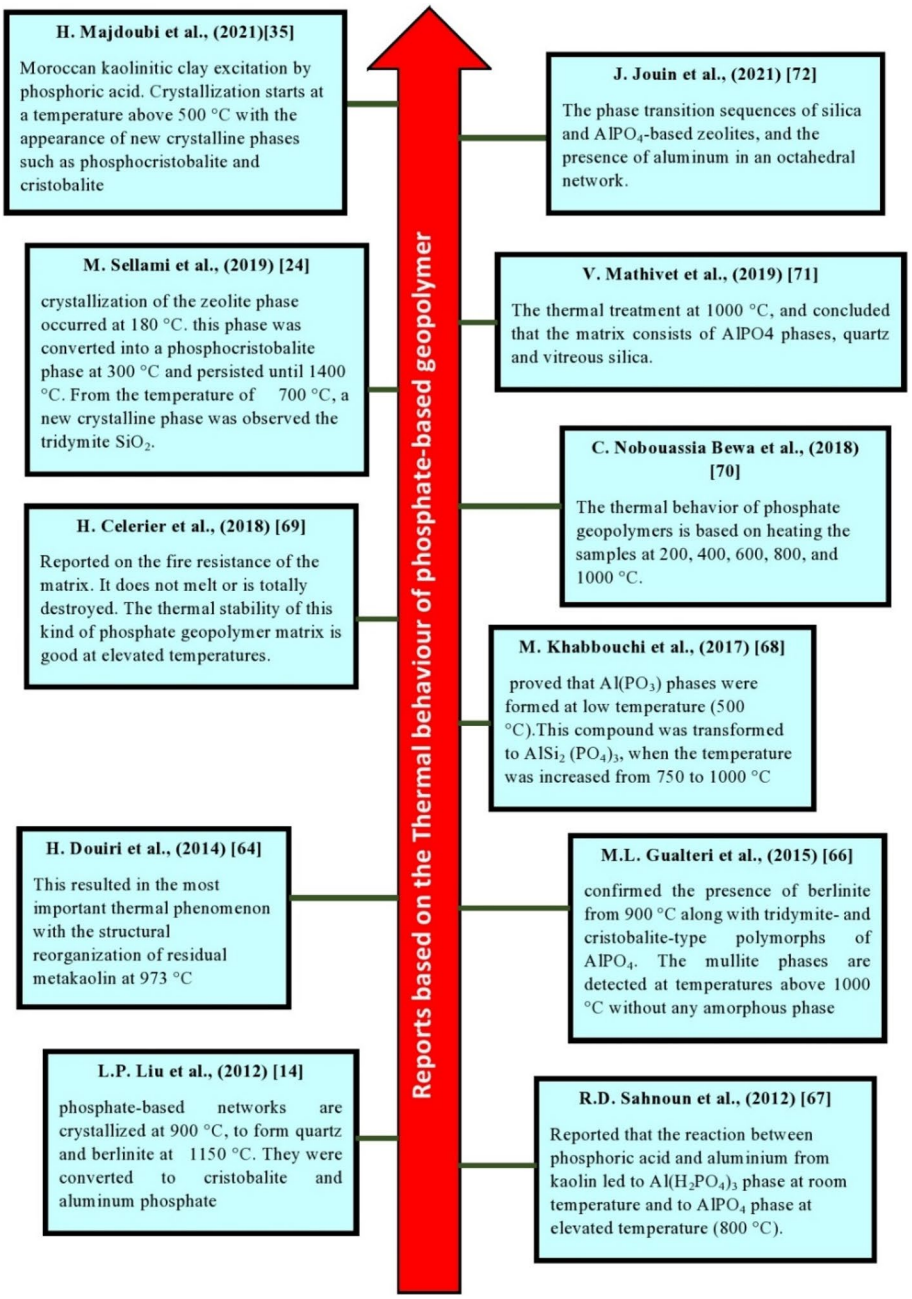

Fig. 1 Literature review based on thermal properties of phosphate geopolymers

particles in cement-based composites, micro-sized additives, which are chemically reactive under geopolymerization, have drawn more attention. The addition of small quantities of micro/nano additives can enhance mechanical performance, thermal resistance, aggressive chemical resistance and lower shrinkage (Dutta et al. 2010; Demirel and Kelestemur 2010; Ping Duan et al. 2017). The expanded application of such composites advances the performance of building materials, such as self-sensing capability, self-healing behaviour, self-cleaning features and low electrical resistivity (Wongkeo et al. 2014; Farahani et al. 2015; Lilkov et al. 2014; Singh et al. 2015).

With reference to reported studies on the potential applications of reactive chemical additives, either silica-based or alumino sources are very limited in metakaolin phospho-cement (Vanitha et al. 2022). This is because the dissolution of silica in acid mainly depends upon the Al/P ratio, and well disintegration of aluminosilicate in acidic pH dominates to form aluminium phosphate. Thus, balancing the reactive and soluble Si or Al from the source materials is quite difficult because of the concurrent dissolution of these in the initial stage to form mainly silico-aluminophosphate gel and aluminium phosphate crystals. Unlike alkali aluminosilicate cement, the effect of soluble silica in the network formation under phosphoric acid is not clearly understood.

In our earlier work (Vanitha and Jeyalakshmi 2023; Vanitha et al. 2022), the effect of nano silica was studied, and the secondary reaction product was established with a more amorphous matrix, established from a broad amorphous halo in XRD reflections between 18 and 32° (2θ) and lower value of the atomic percent of P from EDS results. From NMR data, silicious growth and enhancing the octahedral Al environment without altering the other tetrahedral Al are confirmed. The role of nano silica is assumed to be the transformation of disaggregated Si–OH group under low pH into $Si–OH^{2+}$ and then to $Si–O–Si^{+}$. It is also to be known that acid disintegrates aluminosilicate bonds into Si–O–Si and Si–O–Al, and donor pair of electrons in the oxygen atom take part in establishing a bond with the H^{+} ion released by the acid, which leads to the formation of $(Si)–OH^{+}–(Al)$ units. Owing to the deficiency in the electron density on the oxygen atom, the breaking of this bond releases Al^{3+} ions and Si–OH. As a consequence, Si–O–Si–O–P and an amorphous network of Si–O–Si units are formed with the identified features of crystalline phases of aluminium phosphate.

In view of the above, the present work focuses on the comparison between nano- and micro-sized active silica as a supplementary material for geopolymerization under an acidic medium. Micro form of silica helps to improve geopolymer concrete in an alkali medium through either the pozzolan effect or the filling effect (Mustakim et al. 2021). Silica addition with the free lime throughout the hydration forms C–S–H gel which supplies strength, impermeability and sturdiness to concrete (Autef et al. 2012). Despite their pozzolanic effect, the strength improvement proved in alkali-activated metakaolin (Bezerra et al. 2023), fly ash (Sivasakthi et al. 2018) and GGBS (Saad et al. 1996; Preethi et al. 2020; Krishna Rao et al. 2020; Okoye et al. 2016) in which the Si:Al ratio significantly altered. Published reports indicate their effect on the microstructural properties and guarantee the change of material behaviour to a greater extent in alkali-activated geopolymeric type, but there is no such study on phosphoric-based ones. To fully realize the potential of phosphate-based geopolymer as an innovative material, it is necessary to address the challenges. In view of the above, this research programme aims to investigate the microstructural aspects of phosphate-based geopolymers reinforced with micro silica as an additive and their thermal stability.

Research methodology

Materials used and mixed constituents

Commercially, metakaolin powder and micro silica were obtained from M/s 20 μm limited and M/S Astra Chemicals. MK raw material consists of 52% of oxides of silica and 42% of alumina with less than 2% of CaO. The specific gravity is 2.52 and the bulk density 340 kg/m^3. Orthophosphoric acid (AR grade 85%) was used as an activator solution and was purchased from M/s Southern India Scientific Corporation. Micro silica and nano silica consist mostly of oxide of silica in 99% powdery form. The material mix proportions were optimized after analysing the chemical compositions of the raw materials. XRF: energy-dispersive X-ray fluorescence (EDXRF), 720 Shimadzu, Japan, was used to identify the chemical components present in the form of oxides. The results are presented in Table 1.

Fabrication of the geopolymer samples

To make the geopolymer, metakaolin was chosen as a primary binder (M), and nano (MS) and micro silica (MM) were added additionally in the optimized proportions of 2% (MS2, MM2) and 5% (MS5, MM5). As an acid solution, phosphoric acid 8 molarity has been employed for excitation and also to keep the workability. The control sample (M) and silica admixed specimens were cast by mixing the ingredients in the digi mortar mixer for 10 min followed by the addition of acid solution in a liquid/solid ratio of 0.9 to 1.0. The prepared slurry was poured into a 50-mm cube and was vibrated for 5 min to remove trapped air in between the slurry. The resulting material was wrapped in a polythene sheet to allow the

Table 1 The chemical composition of the metakaolin powder, nano and micro silica with their particle size and charge

Chemical composition (% Wt)	SiO_2	Al_2O_3	Fe_2O_3	TiO_2	SO_4	CaO	K_2O	LOI at 1000 °C	Particle size (nm)	Charge (mV)
Metakaolin	51–53	42–44	< 2.20	< 3.0	< 0.5	< 0.20	< 0.40	< 1	75.8	− 0.3
Nano silica	99.88	0.005	0.001	0.004	–	–	–	0.66	70.6	− 0.1
Micro silica	99.78		0.0002	0.007	0.002	-	-	< 1	150.79	− 5.4

reaction to be completed. The sealed geopolymer matrix was kept at room temperature for 24 h and then cured in a laboratory oven for 8 h at 80 °C to accelerate the polycondensation reaction. Then the cured geopolymer matrix was maintained under ambient temperature for 28 days before testing. The compressive strength of the paste specimens was determined using a digital compressive machine following the ASTM C39-20 standard. An average strength of five specimens has been considered.

Microstructure investigation

The X-ray diffraction (XRD) pattern was collected using a Philips diffractometer model X′Pert using Cu-Kα radiation by scanning from 10 to 80° (2θ) at a scanning speed of 2°/min and at a step size of 0.02°. The particle size and particle charge were determined, employing nanoPartica SZ-100V2 Series. Attenuated total reflectance Fourier transform infrared spectroscopy (ATR-FTIR) spectral study was conducted to study the nature of the fingerprint region and functional group present in the sample using a Shimadzu, IRTracer 100 spectrophotometer with a diamond prism. Absorbance spectra were collected from 4000 to 400 cm^{-1} at a resolution of 2 cm^{-1} and a scanning speed of 5 kHz with 32 scans. Data evaluation and spectra simulation were performed with OPUS software from Bruker. Magic angle spinning nuclear magnetic (MAS-NMR) spectra of ^{29}Si, ^{27}Al and ^{31}P nuclei were recorded using the ECX-400-JEOL 400-MHz High-Resolution Multinuclear FT-NMR spectrometer for solids with a field strength of 9.389766 T (400 MHz). MAS-NMR deconvolution was performed with the Gaussian function. Nuclear magnetic resonances (MAS-NMR) measuring ^{29}Si magic angle spinning (MAS 0 ppm) were performed using TMS as the standard. A pulse width of 2.2 μs and a relaxation delay of 22 s were applied. Acquired solid-state ^{27}Al MAS-NMR spectra were obtained with an external aqueous $AlCl_3$ sample at a concentration of 0 ppm. The ^{31}P MAS-NMR was performed at 0 ppm using orthophosphoric acid. To gain an understanding of morphology, the sample was characterized by field emission scanning electron microscopy (FESEM) using a JEOL JSM 6300 microscope with a tungsten filament electron source and 20-kV accelerating voltage. To ensure that specimens seem to be fully free from water, sample pieces have been hammered from the past's core and dried at 40 °C for 4 h. An X-ray spectrometer (energy-dispersive spectroscopy (EDS)) was employed to determine the chemical compositions of the phases identified. Raman measurement was done with Renishaw via confocal Raman microscope with Linkam hot cell stage and the excitation laser source 532-nm (50 mW) gratings 24,001/mm with the spectral frequency of 100 to 1200 cm^{-1} from RT to 800 °C with 10 mm × 0.2 mm pellet. X-ray photoelectron spectral analysis (XPS) was performed in PHI5600S multi-technique system with Al monochromatic X-ray at a power of 350 W. Al Kα with 10-mA and 15-kV peaks were resolved by the calibration on carbon. The survey scan of the XPS spectrum was done for raw materials and geopolymers in the binding energy range from 0 to 1200 eV.

Thermal properties

Thermogravimetric analysis (TGA/DTA) studies were conducted for a simultaneous thermal analysis (STA) in NETZSCH 2500 Regulus in the temperature range of 30–1000 °C in floating air/nitrogen (60 ml/min) at a heating rate of 10 °C/min. Dilatometry studies were conducted to measure the thermal expansion of the specimens by following a push rod dilatometer method. The samples were heated in a temperature range of 30 to 1000 °C with a constant heating rate of 10 °C per minute. Thermal conductivity was measured using apparatus machine type OSK 4565-A Tokyo Meter Co. Model HVs — 400000SE hot plate method. Temperature in this investigation was varied at RT to 200 °C. High-temperature Raman measurement was done with Renishaw via confocal Raman microscope with hot cell stage and the excitation laser source 532-nm (50 mW) gratings 24,001/mm with the spectral frequency of 100 to 1500 cm^{-1} from RT to 800 °C.

Nano indentation study

Nanoindentation analysis was carried out with NIOS scanning hardness tester with Berkovich tip for load range from 20 to 100 mN. This approach relies on large arrays of nanoindentations analysis of the resulting data. For the nanoindentation process, the basic idea is very simple, initially to push a very sharp tip into the surface

of a material and investigate the mechanical behaviour of the material from the response of the tip. The tip used for this process is the Berkovich tip; it is a three-sided pyramid that is much easier to grind the tip to a point, and thus, it was commonly used in the study of cement-based materials. For the nanoindentation tests, samples were carefully polished to achieve as smooth a surface as possible involving coarse polishing and fine polishing. The methodology reported by researchers like M. Miller et al. (2008) and K. Velez et al. (2001) was adopted here using polishing processes that involve coarse and fine polishing. A microscope examination is used to refer to the sample's smoothness at the end of each procedure.

(i) Coarse polishing process

In the coarse polishing process, the samples were polished carefully with abrasive papers in order (180, 240, 400, 600, 800 and 1200 grit). Each paper was used for 5–10 min. During the coarse polishing process, instead of water, a polishing fluid was used to prevent further hydration of residual geopolymer samples. At the end of each step, a microscope was used to check the smoothness of the sample.

(ii) Fine polishing process

The fine polishing was done with the extra fine alumina suspension consisting of alumina powder and a mixture of ethanol and ethylene glycol at a 1:1 volumetric ratio. At the end of each polishing step, the sample surface was rinsed with ethanol, but not water, to avoid the potential hydration of clay minerals within the matrix. As a result, a highly smooth and flat surface with minimized hydration or wetting of clay minerals was prepared for subsequent nanoindentation testing. Each suspension was used for no less than 30 min.

Finally, the samples were cleaned in an ultrasonic bath for 5 min with alcohol absolute to remove debris and suspensions left on the surface of the samples. Through these polishing steps, the surfaces were smooth enough for nanoindentation tests (Fig. 2).

Results and discussion

Thermo mechanical strength

One of the significant advantages of phosphate-based geopolymers is their significant mechanical strength. Classic alkali-based geopolymers often have a lower compressive strength than phosphate-based ones (Majdoubi et al. 2021). For instance, a comparative analysis made by Tchakoute and Ruscher's (Tchakouté et al. 2017) demonstrated that under the same elaboration conditions, the mechanical strength of a metakaolin-based geopolymer obtained through phosphoric acid activation can reach 93.8 MPa, while that of the same materials obtained through alkaline activation does not exceed 63.8 MPa. The compressive strength values of phosphate-based geopolymers can range from 0.64 MPa (Bai et al. 2017) to 149 MPa (Perera et al. 2008); according to the literature works, the highest possible value has been noted by Parera et al. (2008).

The compressive strength of the prepared metakaolin phosphate geopolymer pastes is presented in Fig. 3b. There is a consistent strength gain in the geopolymers at a standard age of 28 days of curing. Initially, the mechanical performance of phosphate geopolymer M shows 46.2 MPa at 80 °C and is enhanced with the 2% addition of nano and micro silica raised to 58.2 and 51.8 MPa, and with 5% addition, the mechanical performance is further enhanced with 63.6 and 54.2 MPa. This increase in mechanical performance is usually from the gel, and

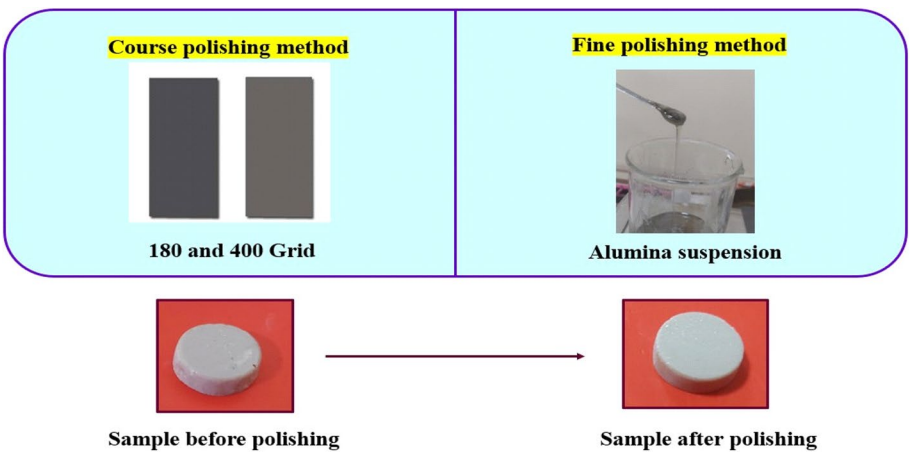

Fig. 2 Sample preparation for the nanoindentation

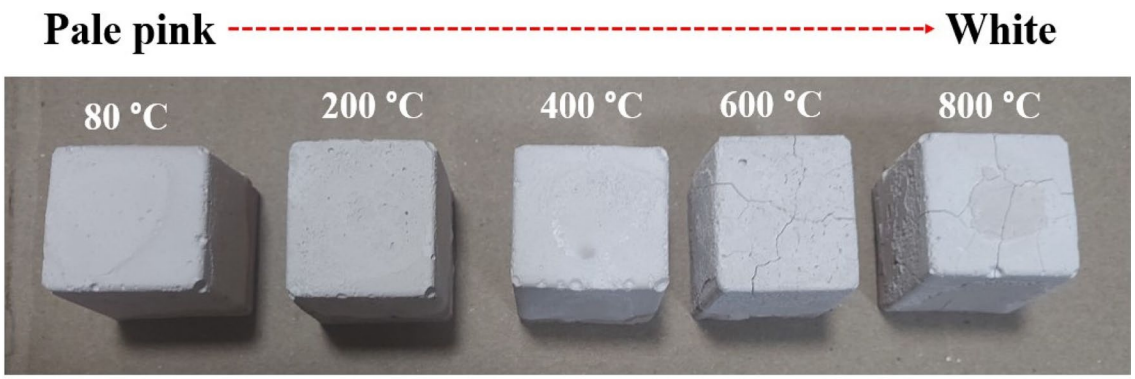

(a): Visual appearance and colour of the sample from 80°C (cured sample) to 800°C

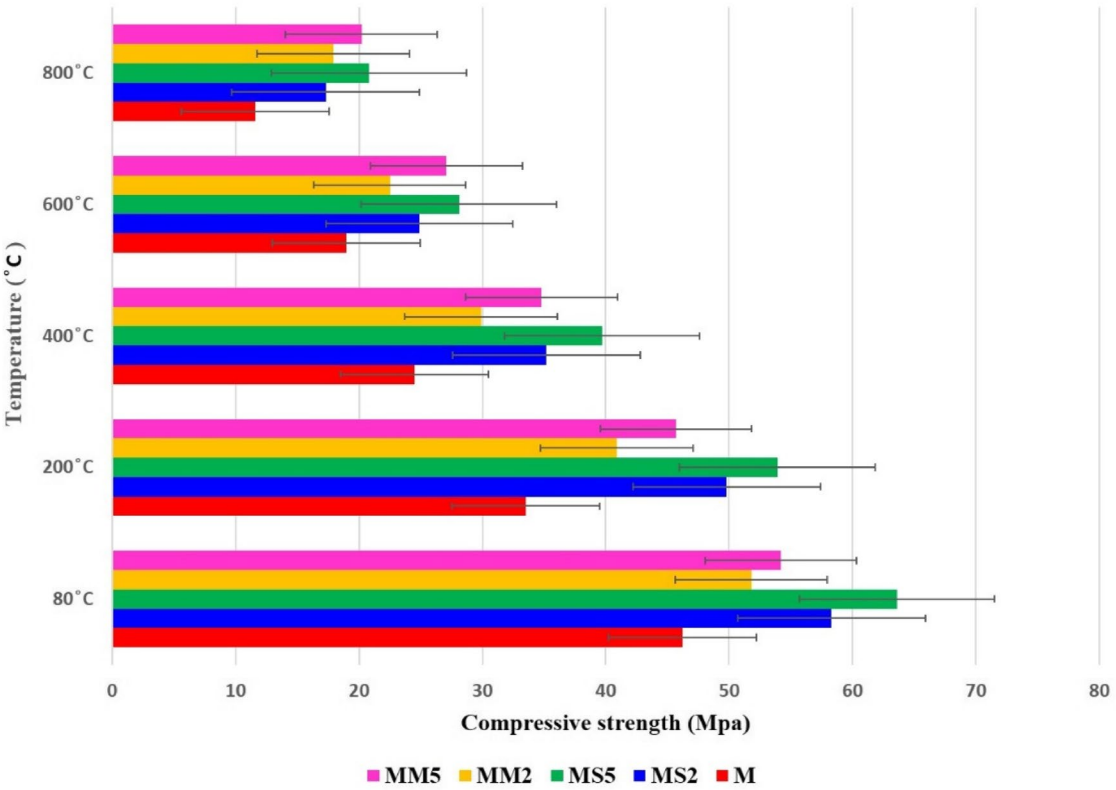

(b): Compressive strengths of geopolymer samples from 80 to 800 ° C

Fig. 3 **a** Visual appearance and colour of the sample from 80 °C (cured sample) to 800 °C. **b** Compressive strengths of geopolymer samples from 80 to 800 °C

crystallite formation by the addition of silica additives is then further explained through nanoindenter.

After exposing the geopolymer matrix at 200 °C temperature for a sustained period of 2 h, the compressive strength decreased to 33.5 MPa for sample M^{200}, 49.8 MPa for $MS2^{200}$ and 40.9 MPa for $MM2^{200}$. While heating hydrated compounds and water molecules, it escaped to some extent. During initial heating at this stage, a slight fall of the compressive strength was obtained in all samples. At this temperature, a visible colour change from pale pink to light pale pink in the sample as shown in Fig. 3a. As the temperature increases at the interval of 200 °C up to 800 °C, the declining trend in strength is found. In the control sample, M^{400} shows

24.5 MPa, M^{600} shows 19.0 MPa, and finally M^{800} shows 11.6 MPa. Partial replacement of metakaolin by micro silica at a smaller dose at a different temperature has shown improved performance as the strength gains are $MM5^{400}$ (34.7 MPa), $MM5^{600}$ (27.1 MPa) and $MM5^{800}$ (20.7 MPa), and by nano silica, it shows $MS5^{400}$ (39.7 MPa), $MM5^{600}$ (27.7 MPa) and $MM5^{800}$(20.8 MPa), thus maintaining the strength of M20 grade, as its compliance with a minimum standard for structural elements. All the samples that were thermally exposed showed a marked colour change from pale pink to white with some physical cracks (Khabbouchi et al. 2017; Liu et al. 2012). Further, microstructural analyses were carried out for samples with a 5% addition of silica using multiple techniques, and the results are discussed in the following sections.

Nanoindentation

The nanoindentation test is used to quantify a material's mechanical characteristics at the nanoscale. Nanoindentation is a straightforward procedure where a known load is applied to the sample's surface using an indenter tip of known form. This technique involves applying a controlled force or load to a sharp indenter tip and measuring the resulting depth of penetration into the material. However, due to the tip's small size and pointiness, a massive amount of pressure which is measured in gigapascals (GPa) will be applied to a particular spot. The area of the residual imprint is computed using the contact depth obtained from the unloading curve after the tip is removed. A sharp indenter tip, typically made of diamond, is pressed into the surface of the material of interest with precise control over the applied force. During indentation, the force applied and the depth of penetration are continuously measured. A load-depth curve with increasing loading, constant holding and decreasing unloading is produced by continually recording force and depth during loading, holding and unloading, respectively. This data is used to create a load–displacement curve, which provides information about the material's micromechanical properties. (Oliver and Pharr 2004; Pharr and Bolshakov 2002) method is generally applied to derive the important mechanical characteristics, namely elasticity E and hardness H, using the load depth (p–h) curve. The methodology and model graph have been represented in Fig.4.

The two key parameters are measured through nanoindenter:

(a) Hardness: Nanoindentation provides a measure of the material's hardness, which is its resistance to deformation. It is an important property for characterizing materials' ability to withstand wear and indentation.

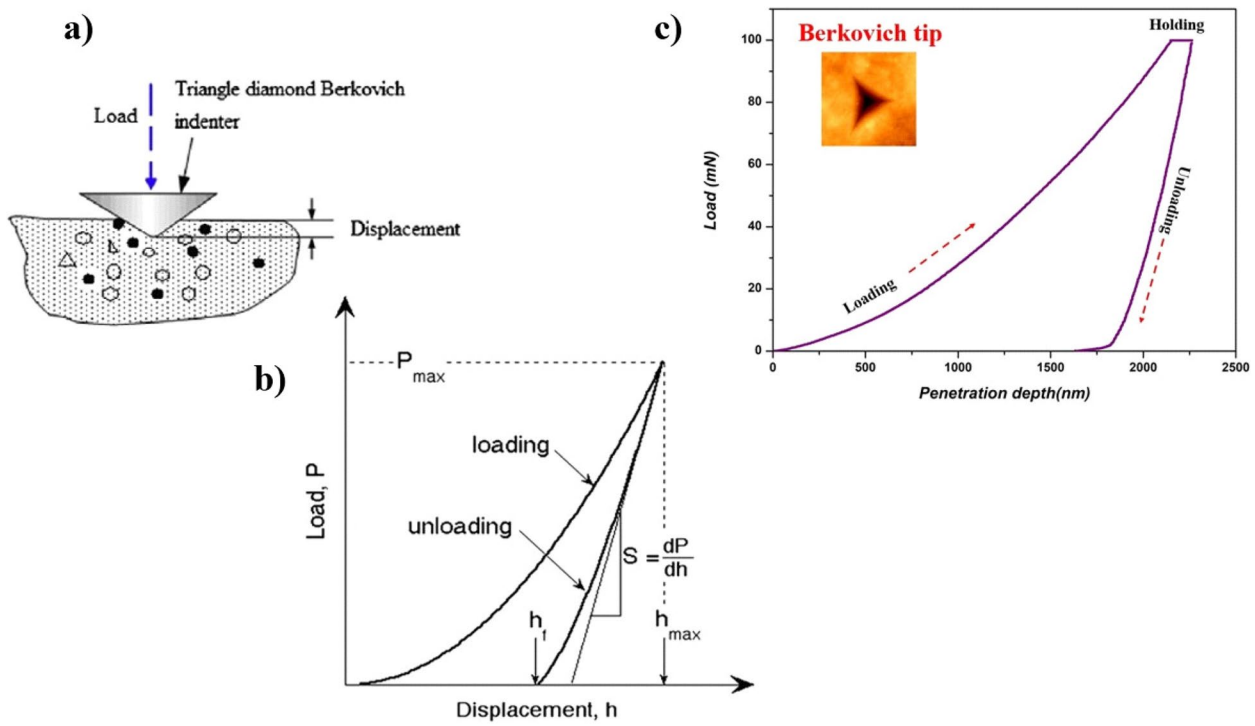

Fig. 4 Graphical representation of the indentation process and outcome graph

(b) Elasticity: Nanoindentation also measures Young's modulus, which quantifies a material's stiffness or elasticity. It describes how a material responds to deformation under an applied load.

The accuracy of p–h curve measurements relies on determining three key quantities: maximum load (P_{max}), maximum displacement (h_{max}) and (S=dP/dh) elastic unloading stiffness (Oliver and Pharr 2004; Pharr and Bolshakov 2002). The three-sided pyramidal Berkovich tip made up of a diamond with a diameter of around 100 nm and a contact angle of 65.30 is used for indentation.

Hardness H is computed using the area function and maximum load; after the contact area is established, the hardness is evaluated using the following:

$$H = \frac{P_{max}}{A} \tag{1.1}$$

The contact area under load serves as the basis for the definition of hardness; if there is a large amount of elastic recovery after unloading, the traditional hardness measurement from the area of the residual hardness impression may differ. But usually, this only matters for materials with incredibly low E/H values.

The initial slope of the p–h curve determines the elasticity of the sample which can be calculated as follows:

$$E = \left(1 - \nu^2\right)\left[\frac{1}{E_2} - \frac{(1 - \nu_i^2}{E_i}\right]^{-1} \tag{1.2}$$

where E and ν are Young's modulus and Poisson's ratio for the sample, E_i and ν_i are the same parameters for the indenter and E_i=1140 GPa and ν_i=0.07 for the diamond indenter.

The depth-sensing indentation method produces a load–displacement curve from which microhardness and elastic modulus can be derived using a variety of approaches. Instrumented indentation, referred to as nanoindentation at low loads and low depths, has now become established for the single-point characterization of hardness and elastic modulus of both bulk and coated materials. Generally, it is a good technique for measuring the mechanical properties of homogeneous materials but applied recently to probe different types of phases like gel phase and hard crystalline materials in geopolymers (Oliver and Pharr 2004). For the very first time, this technique is applied to a phosphate-based geopolymer to verify the changes that occurred during the phosphate attack.

As multiphase composite materials, cementitious binders are comprised of, unreacted particles, impurities, pores and different products at micro and nano scale. Given a material attribute (either microhardness H or elastic modulus E), a probability density function for each component phase can be used to characterize the cementitious binder, which can be thought of as a superposition of product phases. It is also possible to express in terms of the probability distribution of each state as well as the possibility that it is that specific state among the others. This is directly related to the indentation depth choice, which was made to make it suitably small in comparison to the typical length of the microstructural heterogeneities (Kong et al. 2012; He et al. 2013; Puertas et al. 2011; Němeček et al. 2009). From the previous literature reports, it was clear that this technique will be useful in identifying the type of gels formed during the hydration in the case of OPC and polycondensation in aluminosilicate precursors. The value mostly falls in the range$E$=2–31 GPa and H=0.7–1.7 GPa for typically C-S–H gel phase in cement, whereas it is slightly higher in alkali-activated matrix with E=11.3–17.1 GPa for N-A-S–H gel and E=18–34-GPa C-A-S–H gel (Němeček et al. 2011; Lee et al. 2016; Luo et al. 2021).

Corresponding to each indentation point, a typical load–depth curve was generated from the loading history by increasing the loading. The methodology applied here is increasing the load stepwise from constant value and then holding followed by unloading. From the initial slope of the elastic unloading in the load–depth curve, the mechanical parameters, elasticity E, hardness and H are calculated. From the established mechanism, it is understood that metakaolin phosphate geopolymer consists of aluminium phosphate as an X-ray crystalline phase, silicophosphate and silico-aluminophosphate gels in an amorphous phase along with unreacted metakaolin, and a few SiO_2phases is explained further in the following sections. Typical loading–displacement curves in an identical indentation depth of different nanometres are used to identify these phases in the matrix (Hu et al. 2014).

The obtained curves for geopolymers M, MS5 and MM5 under classical nanoindentation methodology at different loads ranging from 20 to 100 mN are presented in Fig. 5. For each load, about 50–60 intenders are made, and the average has been considered. The nature of the loading and unloading curves is found to be nonlinear. The corresponding positions are considered to probe the micro images through an optical microscope and presented in Fig. 5.

The curve of sample M at loads 20, 40 and 60 shows a regular pattern, whereas loads 80 and 100 show a slight displacement in Fig. 6. The typical curves are analysed at different locations and concluded that the product consists of a gel phase as well as some crystallites. The range

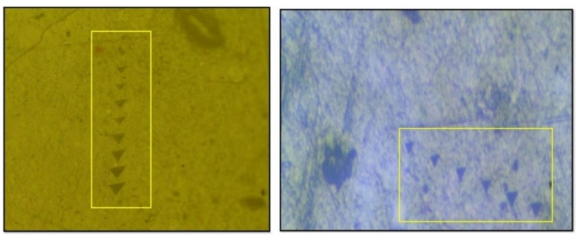

Fig. 5 Optical images of identified place used in classical nanoindentation

of elastic modulus and hardness values of the different constituents of concrete can be found in the literature (Nuruzzaman et al. 2023; Sorelli et al. 2008; Shaikh et al. 2017). Since the paste samples are used for investigation in this study, the hardness and elastic modulus values are low compared to those for aggregates that are found in the range > 5 GPa and 75–100 GPa, respectively. In our study, the hardness value lies in the range of 0.9 to 1.3 GPa which corresponds to the gel phase as verified from the reported literature (Díaz-Pérez et al. 2021). The elasticity value ranges between 31.9 and 43.7 GPa which are from generally heterogeneous phases (Deb et al. 2022; Mondal et al. 2010).

For sample MS5 for every load, an irregular pattern was observed in the p–h curves. This is due to the lower and higher gel phase associated with the geopolymer matrix. From other analytical techniques, it is found that the MS5 sample has silicophosphate gel, aluminium phosphate gel and crystals. The loads from 20 to 40 mN confirm the presence of the lower density gel phase with the hardness and elasticity values of about $H = 0.5 \pm 0.39$ and $E = 10 \pm 4.9$ GPa which was found to be lower compared to the M sample. The hardness value of all the loads shows a range of 0.3 to 1.5 GPa which is of gel phase. Elasticity values range from 8.4 to 66.2 GPa which has a low-density and high-density gel, partially active phase and crystal grains. In all the loads, a mixture of lower- and higher-density gels is found so the p–h curve as it is slightly deformed.

While looking at the curves for MM5 as described in Fig. 6, slight displacements in the curves were found, and most importantly, the marginal increase in elastic modulus was obtained in all ranges of load applied. MM5 sample shows more of a partially activated phase along with crystal grains, whereas the hardness and elasticity are higher ranging from $H = 1.5 \pm 0.26$ GPa and $E = 57 \pm 3.0$ GPa. This also coincides with the bulk mechanical property. From the literature, a higher value was observed when partially activated, and crystal grains were found in the sample which has values > 30.0GPa (E) and > 5.5GPa (H); it also coincides with the micro silica-induced phosphate geopolymer. Compared with nano silica, the micro silica-infused sample shows some crystal grains which are discussed further in SEM analysis. The addition of nano and micro silica improved the microhardness of the network of metakaolin at a small dose of 5%. This is also matched to the bulk mechanical performance (Morales et al. 2015; Zyganitidis et al. 2011). Reported alkali-activated FA and MK have low-density C-S–H gel in the range of 16 ± 2.4 (E) and N-A-S–H in the range of 4.4–16.8 GPa (E). Comparing this, a higher-density gel phase with 21–30.4 GPa was reported in this current study. Thus, metakaolin excited by acid is more advantageous than alkali excitation in terms of both micro- and macro-level performance. The microstructural properties are explained in further sections.

X-ray diffraction analysis

XRD patterns of raw materials

The mineralogical phases are determined by XRD before and after thermal treatment. Metakaolin source material possesses a hexagonal layer as it retains a long-range order. It shows a typical halo of the amorphous phase between 18 and 32° (2θ) with a characteristic reflection of illite (11° and 19° (2θ)), quartz (22° (2θ), anatase (25°) and hematite (36°) phases identified from PDF (02–0056), PDF (74–1811), PDF (21–1272) and PDF (33–664) which is depicted in Fig. 7a. Nano silica is mostly composed of amorphous quartz (S), and micro silica shows crystalline patterns of quartz despite the high fineness of the particles; the XRD reflections are obtained at 21.0, 26.9, 36.8, 39.7, 50.3, 60.2 and 68.6° (2θ) PDF (74–1811) shown in Fig. 7b.

XRD patterns of geopolymer samples

The results obtained from XRD analysis of geopolymer samples before heat treatment M and silica-added MM5 and MS5 show an amorphous halo between 20 and 30° 2θ (M) and at 19 to 34° 2θ for MM5 and 18–32° (2θ) for MS5. Aluminium from metakaolin forms berlinite (PDF 10–423) phases upon phosphoric attack, and corresponding reflections appeared along with quartz in both before-heat samples. Some forms of aluminium phosphate reflections that are seen at 2θ values of 20°, 25°, 27°, 29°, 35° and 38° attributed to berlinite, and reflections at 60° and 62° attributed to a hydrated form of aluminium phosphate ($Al(H_3PO_4)_2.3H_2O$) (PDF 00–020-0010), while illite phases in MK are retained in the M geopolymer sample shown in Fig. 8a. This could be explained since the geopolymerization of aluminosilicates activated by phosphate usually involves the dissolution and reconstruction of silicates, aluminates and phosphates to form disordered silicophosphate (S-P), aluminophosphate (A-P) and/or silico-aluminophosphate (S-A-P) gels, which are typically amorphous phases. It is also to be

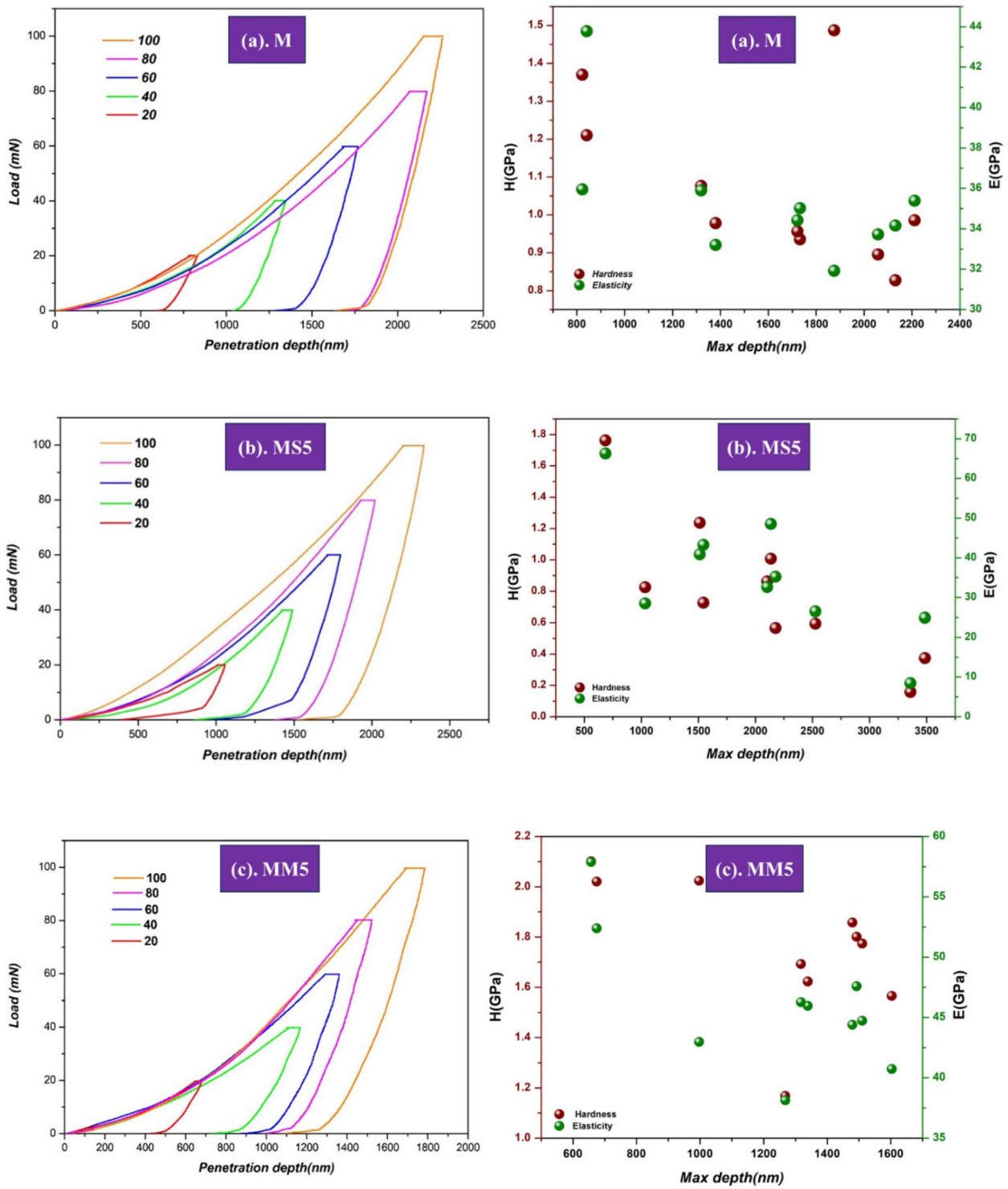

Fig. 6 Load depth curves and hardness and elasticity of phosphate geopolymer samples **a** M, **b** MS5, and **c** MM5

noted most of the quartz-based reflections as observed in micro silica declined in MM5 geopolymer with additional quartz phases, which is related to raw micro silica. A sharp peak at 28° in MM5 is attributed to the quartz phase (Khabbouchi et al. 2017; Sellami et al. 2019)(Sahnoun and Bouaziz 2012) .

After thermal treatment from 200 to 800° C, all X-ray patterns of geopolymer cement M^{200} to M^{800}, $MS5^{200}$

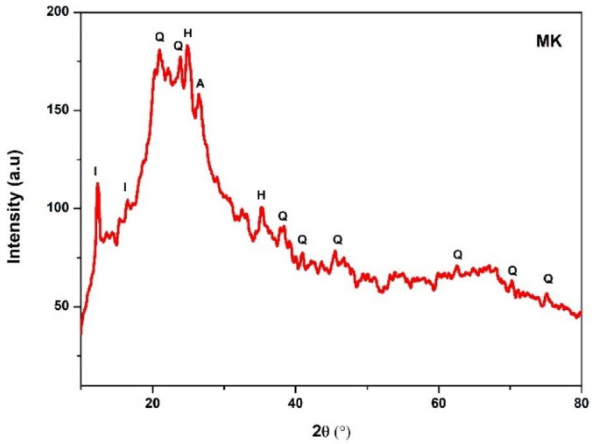

(a): XRD of metakaolin

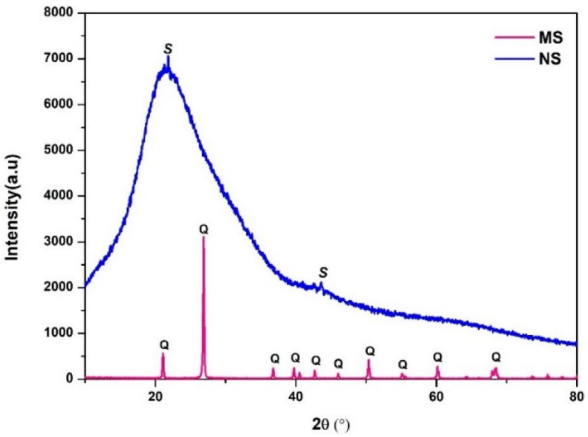

(b): XRD of nano silica and micro silica

Fig. 7 **a** XRD of metakaolin. **b** XRD of nano silica and micro silica

to $MS5^{800}$ and $MM5^{200}$ to $MM5^{800}$show changes in the X-ray pattern mainly due to the depolymerization of the 3D poly(phospho-siloxane) – Si–O–P–O–Si networks formed during the reaction. We are here to state that nano silica as an additive fully reacted during the reaction, and upon heating, silica phases undergo thermal reaction to form quartz phase. In general, the results show that the de-silication of poly(phospho-siloxane) bond is due to the thermal transformation of metakaolin geopolymer (Mathivet et al. 2019; Celerier et al. 2019). Accordingly, while heating this poly(phospho-siloxane) bond breaks, more of aluminium phosphate phases that were found provide the mechanical strength. But we also observed peaks at 21.9, 31.2, 33.2, 35.8, 41.1 and 60.9 (2θ) from phosphocristobalite (P) (00–011-0500) and SiO_2phases with the sharp intensity peaks at 20.5, 26.5 and 64.7 (2θ) as tridymite (T) (01–070-4689) The amorphous halo has been reduced upon heating from 200 to 800° C in all samples (Celerier et al. 2018; Sellami et al. 2019; Liu et al. 2012). Comparing the control with micro silica-added samples, the intensity of quartz form phases intensified upon heating is further explained by TGA-DTA.

Thermogravimetric analysis and differential thermal analysis

TGA-DTA was carried out from room temperature to 1000 °C to assess the heat of evaporation and mass loss. The thermograms are presented in Fig. 9a and b. While heating, physically bonded water, chemically bonded water and hydroxyl groups are eliminated, and hence, there is a mass loss in TGA curves. The TGA curves of M, MS5 and MM5 show endothermic peaks, in the first, under a temperature range between 25 and 100 °C. The major mass loss in this region was due to the evaporation of water from the materials known for physically bonded water. The mass loss is about 15% in M, 6.3% in MS5 and 4% in MM5, at this temperature region. Below 100 °C a part of physically absorbed water and one part of the chemically bound water in the poly(phospho-siloxo) network is removed (Wang et al. 2017; Katsiki et al. 2019; Tchakouté et al. 2017; Hui et al. 2021).

The second region related to chemically bonded water between the temperature range 100–300 °C is attributed to the evaporation of structural water, but the loss is meagre. It showed as an endothermic peak suggesting a strong geopolymerization reaction; this also evolves over time resulting in higher consumption of water in the material. Consequently, those weight losses are due to metastable phases which are free water that can be linked to hydrated aluminophosphates in acid activation. We found that the total mass loss from the TGA thermogram is about 25.4% in M, 17.2% in MS5 and 15.8% in MM5. The third region lies above 300 °C temperature due to the hydroxyl group evaporation. This is from hydroxyl groups from P–OH as a result of the H_3PO_4 reaction with aluminosilicates. The total mass loss in M is about 25.4% which is reduced much in MM5 at 15.8% (Fig. 9) (Sellami et al. 2019; Liu et al. 2012).

In DTA, a peak at 119, 120 °C in M and MS5 and 127 °C in MM5 temperature observed is related to the volatilization of adsorbed water, counting the mass loss of 17% and 15%. The mass in hydroxyl water molecules was mainly lost at temperatures below 500 °C mainly from interlamination between the Al–O and Si–O layers. The exothermic thermal event, observed at 500–700 °C, was assigned to the crystallization of the amorphous matrix into cristobalite and tridymite-type structures in both samples.

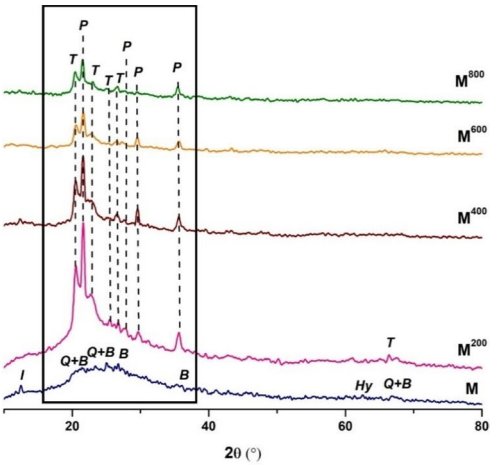

(a): XRD of sample M before and after thermal treatment

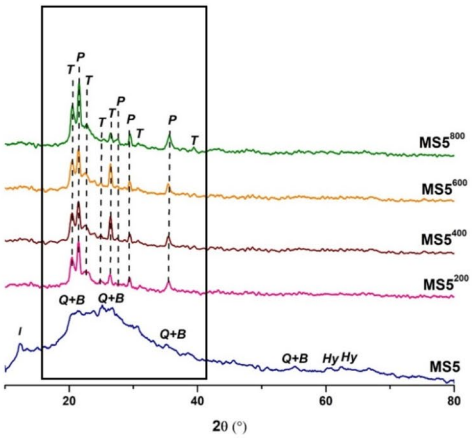

(b): XRD of sample MS5 before and after thermal treatment

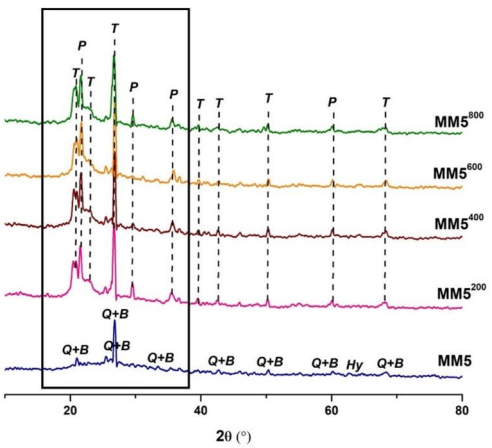

(c): XRD of sample MM5 before and after thermal treatment

◀ **Fig. 8** **a** XRD of sample M before and after thermal treatment (B, berlinite phase of aluminium phosphate; Q, quartz; P, phosphocristobalite; T, tridymite). **b** XRD of sample MS5 before and after thermal treatment (B, berlinite phase of aluminium phosphate; Q, quartz; P, phosphocristobalite; T, tridymite). **c** XRD of sample MM5 before and after thermal treatment (B, berlinite phase of aluminium phosphate; Q, quartz; P, phosphocristobalite; T, tridymite)

The chemical phase changes arose from the gradual formation of Al $(PO_3)_3$ phase from $(Al(H_2PO_4)_3)$ according to the following reaction:

$$P_2O_5 + Al_2O_3 \rightarrow 2AlPO_4 \quad (1)$$

In the case of MM5 samples, we observed small peaks at different temperatures above 550 °C and in MS5 above 700 °C. These can be accounted for by the following transformations: amorphous aluminium phosphate and silicophosphate phase into crystal phase tridymite-like molecular structure at around 700–870 °C. It might be due to more quartz phase in MM5. The features at 800 to 870 °C, respectively, show exotherms in the DTA data but no notable corresponding mass loss and so are likely to relate to phase transitions in the newly formed binder gel. These may be assigned to the amorphous aluminium phosphate phase transforming into trigonal(alpha-$AlPO_4$) and tetragonal (beta-$AlPO_4$) berlinite at elevated temperatures, which are all exothermic processes. The peak that appears at 943 °C and 989 °C is the characteristic of the crystallization into mullite of the unreacted MK (Douiri et al. 2014; Liu et al. 2012; Allahdin et al. 2016).

Attenuated total reflectance Fourier transform infrared spectroscopy

Metakaolin, being aluminosilicate one, can observe the IR frequency absorption bond corresponding to Si–O–Si and Si–O-Al stretching and deformation vibrations at 1058 and 1029 cm^{-1}, respectively. The bands at 790, 673, 599 and 555 cm^{-1} are assigned to quartz of Si–O and Si–O–Al stretching and amorphous silica phases respectively. The spectra of the hardener, phosphoric acid, show a broad peak at 3306 cm^{-1} due to the vibration of O–H bonds. Some absorption bands near 2345 cm^{-1}, 1638 cm^{-1} and 1158 cm^{-1} are from bound water molecules of (H–O–H) stretching from phosphoric acid. The deprotonation of H_3PO_4 into HPO_4^{2-} ions is confirmed by the observed peak at 987 cm^{-1}. Nano silica shows a band near 813 cm^{-1} derived from Si–O–Si symmetric stretching. The asymmetric stretching vibrations of SiO_4 observed at 1101 cm^{-1} correspond to the Si–O–Si bond vibrations. Micro silica shows a sharp Si–O–Si stretching

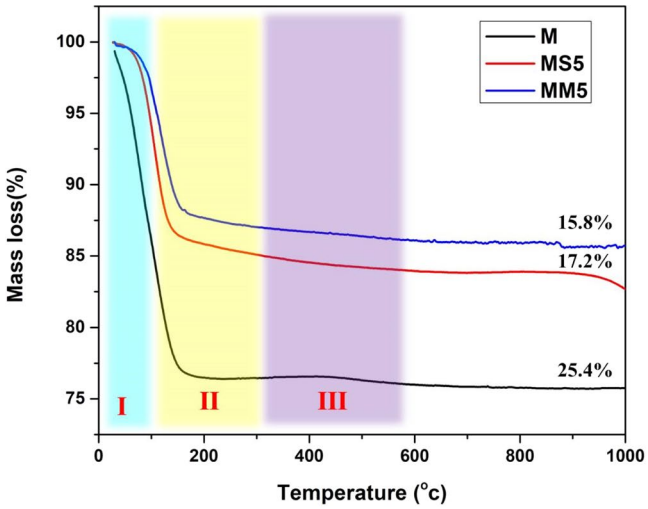

(a): Thermal analysis of phosphate geopolymer sample M,MS5 and MM5

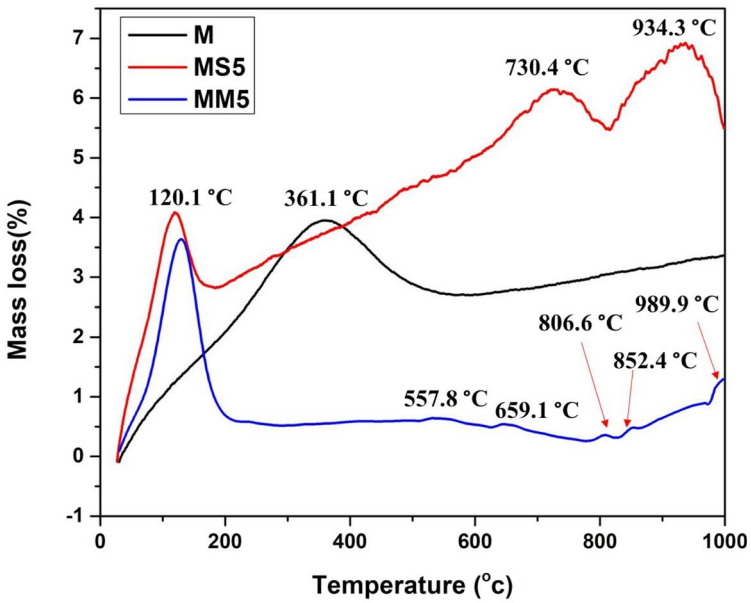

(b): DTA analysis of phosphate geopolymer sample M,MS5 and MM5

Fig. 9 **a** Thermal analysis of phosphate geopolymer sample M, MS5, and MM5. **b** DTA analysis of phosphate geopolymer sample M, MS5, and MM5

band at 1068 cm $^{-1}$ along with Si–O, Si–O–Si and quartz at 459, 512, 702 and 773 cm $^{-1}$, and these networks also coincide with the XRD patterns of micro silica.

Asymmetric stretching vibrations are seen at 1033 and 1066 cm^{-1} which are from the shifting of peaks 1029 and 1058 cm^{-1} from metakaolin in which they are the characteristic of the Si–O–Si/Si–O–Al link in the Q^2 and Q^3 environments. These vibrational frequencies are keenly observed on thermally treated samples where they correspond to a single peak to 1059 cm^{-1} in M^{200}, 1065 cm^{-1} in M^{400}, 1071 cm^{-1} in M^{600} and 1083 cm^{-1} in M^{800}. This major geopolymer fingerprint region experiences redshift where it is shifted to a higher wavenumber (Tchakouté et al. 2017; Zribi et al. 2020).

In Table 2, a newly appeared peak at 910 cm^{-1} is assigned to P–O–P vibration due to the excess of PO_4^{3-}ions which are not involved in the geopolymerization reaction (Abdel-Kader et al. 1991; Izci 2014). It has

Table 2 FTIR of raw materials and geopolymer before and after heat treatment

ATR-FTIR SPECTRUM OF RAW MATERAILS

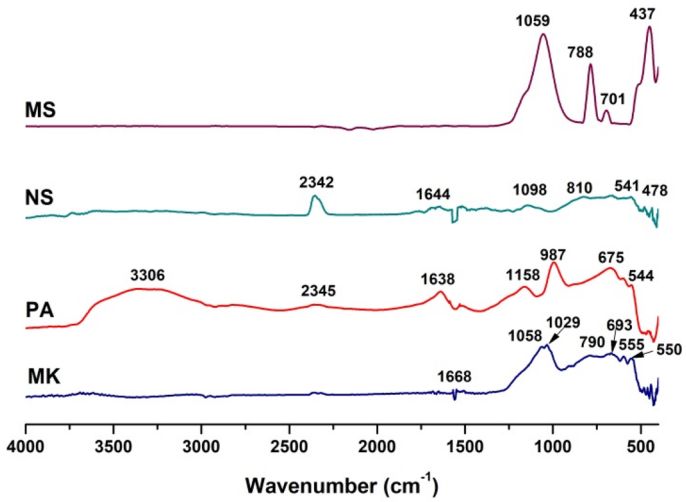

ATR-FTIR SPECTRUM OF CONTROL SAMPLE

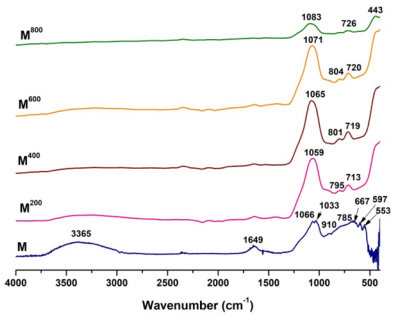

ATR-FTIR SPECTRUM OF NANO SILICA AND MICRO SILICA INCORPORATED SAMPLE

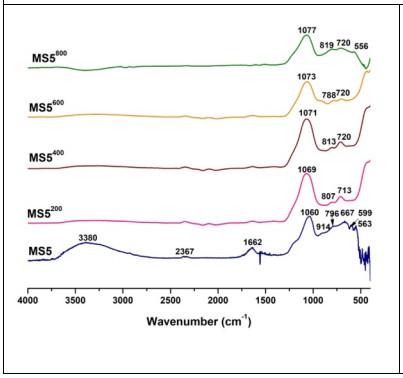

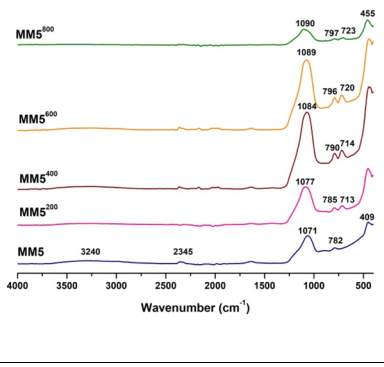

disappeared during the thermal treatment. The appearance of bands at 785 cm^{-1} is a symmetric stretching which corresponds to the Si–O–P network after the acid attack. Upon heating a 200 °C, this peak appeared as a doublet at 795 and 719 cm^{-1}. Further, shifting to lower wavenumber 719–720 cm^{-1} in M^{400} and M^{600} showed a red shift at 726 cm^{-1} at elevated temperature 800 °C exposure (M^{800}) assigned to Si–O–P. The other bands like 597 cm^{-1} of AlO_6 vibration showed a higher wavenumber shift, blue shift in M compared to metakaolin. Most of the Si–O bands are broad due to the distortion of the tetrahedral and octahedral layers. In the lower region of IR frequency, one can see the peaks of Si–O–Si symmetric stretching vibration along with Si–O stretching vibration nearly at 553 and 667 cm^{-1}. These bands disappeared after thermal treatment (Celerier et al. 2019, 2018) (Nobouassia et al. 2018). The observed quartz peak at 800 °C corresponds to 443 cm^{-1} and coincides with XRD pattern.

The sample MS5 has distorted tetrahedral and octahedral layer present in MK that is seen through a vibration band at 1060 cm^{-1}. At 200 °C ($MS5^{200}$), this peak shifted to 1069 cm^{-1} and finally reached at 1077 cm^{-1} at 800 °C ($MS5^{800}$). Thus, it is clear during the condensation reactions that amorphous silica contributes to the formation of hydrated alumina silicates in addition to alumino silicophosphate phases with almost negligible quartz phases. But silica-dominated micro silica addition (MM5) made a higher frequency shift of the major peak at 1071 cm^{-1} at higher intensity compared to other samples M, MS5 and MM5 as shown in Table 2. It is similar to the Si–O–P phase reported on metakaolin activation with natural silica source by M. Khabbouchi et al. (2018) (Jouin et al. 2021) in the range of 1025 to 1165 cm^{-1}.

Raman spectra

Raman spectra were studied in the range of 100 to 1200 cm^{-1}. The spectra in Figs. 10 and 11 show the vibrational bond characterization, and MK was an amorphous material; thus, Raman spectra do not reveal more information about various phases due to their amorphous nature. Raman spectra of MK have networks of Si–O stretching vibration which has some sharp peaks at 141 cm^{-1}. The major network in metakaolin is T–O–T (T = Si or Al) which is seen at a range of 400 to 580 cm^{-1} with some sharp peaks at 980 to 1200 cm^{-1}. Some Al contributions of AlO_6, Al–O bending and Al_2O_3 vibration are found at 327, 730 and 818 cm^{-1}in metakaolin (Ettoumi et al. 2023). The micro silica (MS) has a crystalline nature and shows a strong sharp peak of Si–O in the range between 170 and 200 cm^{-1} and Si–O–Si at 462 cm^{-1}. Quartz and SiO_2 bending vibration of Si–O–Si were found at 634 and 699 cm^{-1}. Nano silica (NS) has Si–O–Si bending vibration at 441 cm^{-1} with sub-peaks

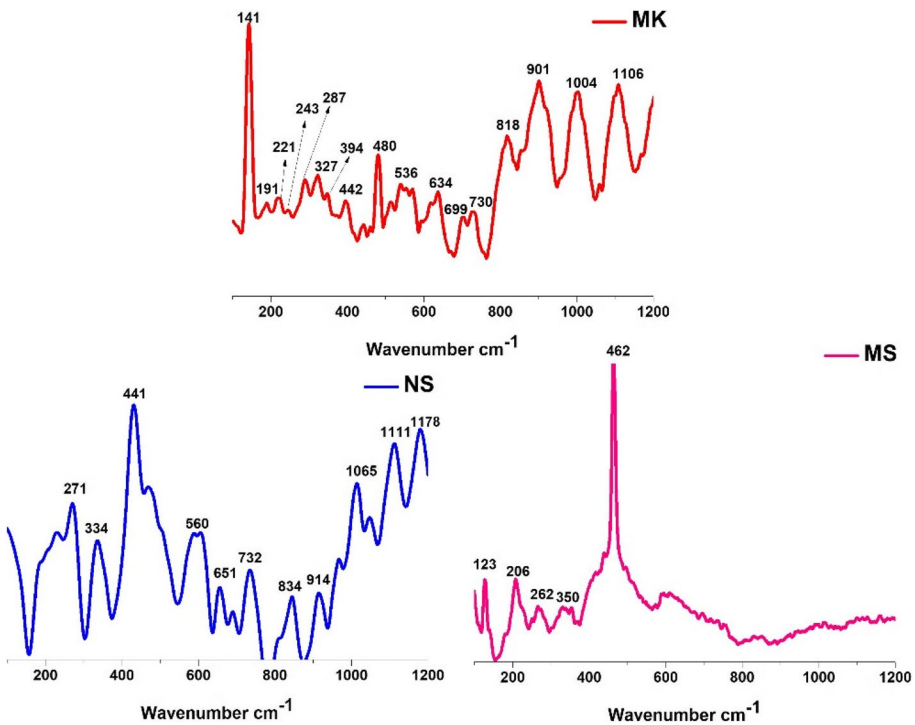

Fig. 10 Raman spectra of raw materials

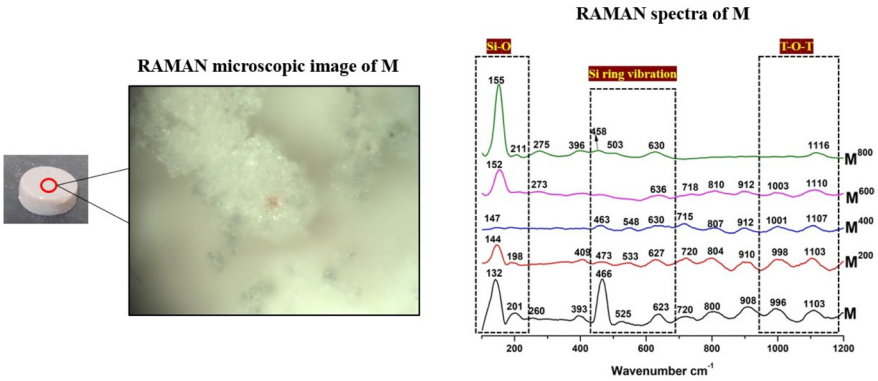

(a) : In-situ high-temperature Raman spectra of sample M

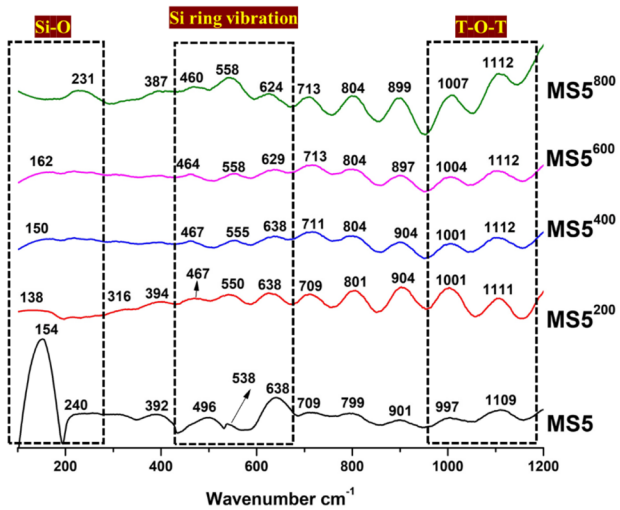

(b): In-situ high-temperature Raman spectra of sample MS5

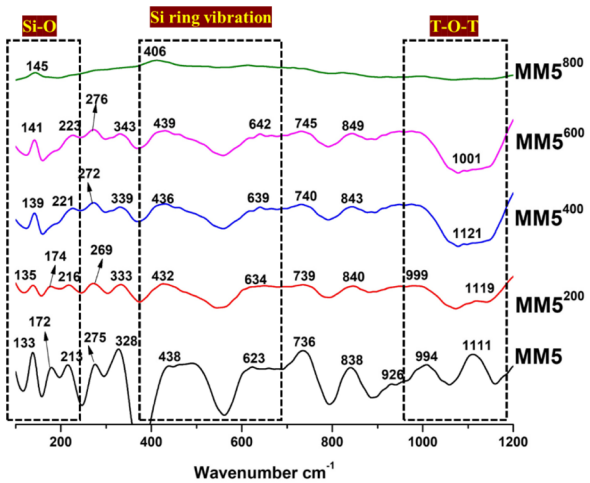

(c): In-situ high-temperature Raman spectra of sample MM5

Fig. 11 **a** In situ high-temperature Raman spectra of sample M. **b** In situ high-temperature Raman spectra of sample MS5. **c** In situ high-temperature Raman spectra of sample MM5

of 651 and 1065 cm^{-1}. The major network in metakaolin is Si–O–Si and Si–O–Al which is seen at a range of 400 to 580 cm^{-1} with some sharp peaks at 980 to 1200 cm^{-1} (Fig. 10).

In situ high-temperature Raman spectra

Raman spectroscopic data are consistent with FTIR data. In situ studies were carried out for geopolymer samples M, MS5 and MM5 from a temperature range from ambient temperature to 800 °C. At ambient temperature, the major Si–O peak from metakaolin 141 cm^{-1} has been shifted to a lower wavenumber at 132 cm^{-1} in M as temperature increases from 200 to 800 °C. This stretching vibration has been shifted higher wavenumber from 132 to 201 cm^{-1} as shown in Fig. 11a. This is due to the Si network bonded with the hydroxyl group as a result the silica gel formed with aluminosilicate with acid. After high-temperature exposure, Si–O has been changed to SiO_2 phases; this is also explained in XRD by the tridymite phase. The aluminium-connected phosphate groups were identified from the region between 260 and 396 cm^{-1} as Al–O or Al–O–P bending vibration. Upon acid attack, the primary reaction of the dealumination arose from the reaction between aluminosilicate and acid, and the Al–O deformation changed into Al–O–P networks. This can be obtained by a shift in the range between 260 and 409 cm^{-1}due to Al–O–P bending along with Si–O–Al stretching vibration (Ettoumi et al. 2023; Keeley et al. 2017).

In the MS5 sample, a broad peak was observed at 150 to 220 cm^{-1} due to the amorphous form of nano silica incorporation. A major Si–O–Al stretching vibration is observed in the range of 316–394 cm^{-1}. Figure 11c represents the sample MM5, which has a peak at 133 cm^{-1} and has been constantly shifted to a higher wavenumber due to the presence of crystalline Si content which reaches up to 145 cm^{-1} in $MM5^{800}$. In addition, some minor peaks at 172 and 174 cm^{-1} in MM5 and $MM5^{200}$ appeared slowly suppressed, while the temperature increased from 400 to 800 °C. Similarly, the appearance of Al–O–P bending vibration at 275 cm^{-1} at ambient curing had shift to a slightly higher wavenumber upon the thermal treatment which reaches up to 223 and 276 cm^{-1}at 600 °C and is absent at 800 °C (Mierzwiński et al. 2019; Zhang et al. 2017).

The T–O–T peaks appeared in the following range at different samples: In M, a peak is in the range 458–503 cm^{-1}, MS5 in 460–558 cm^{-1} and finally MM5 402–438 cm^{-1}. The transformation of Si–O–Si to SiO_2 bond at elevated temperature shifts the corresponding frequency band from 600 to 647 cm^{-1}wavenumber in all geopolymer samples (Ettoumi et al. 2023; Tanwongwan et al. 2020). An Al–O bending vibration at 730 cm^{-1} in MK shifted to a lower wavenumber in control sample M 715–720 cm^{-1} which indicates that the control sample is an amorphous system. On the other hand, in the micro silica-added sample, it is shifted to a higher wavenumber number 736 to 745 cm^{-1} due to the crystalline pattern of incorporated silica source. At the same time, the amorphous nano silica in this band appeared, and it ranges from 709 to 713 cm^{-1} which is much lower.

The analysis of Si–O–T (T=Si, Al or P) symmetric stretching vibration has been done to check the thermal transformation of the main geopolymeric reflections. It can be seen in the region between 950 and 1200 cm^{-1} as the temperature increases; a higher shift of this band is a clear indication of the thermal reaction of aluminium phosphate berlinite form. According to that the Si–O–T frequency is almost in the range of 996 to 1103 cm^{-1} respectively in sample M at ambient temperature slowly shifts to higher wavenumber to 1003 and 1110 cm^{-1} at 600 °C and single peak at 1116 cm^{-1}at 800 °C (Keeley et al. 2017; Stefanovsky et al. 2016). It is in line with stage-wise desilication, dehydroxylation and dehydration process. The same has been identified in other additive-added samples (Rokita et al. 2000; Khabbouchi et al. 2018). The higher shift is seen in the MM5 sample with a maximum of 1121 cm^{-1}. Thus, XRD reflections and Raman analysis conform to the bond disruptions during the thermal exposure and formation of Al–O/Si–O linkages in phosphocristobalite or tridymite phases. The presence of crystallinity in the geopolymer matrix was believed to positively contribute to the compressive yield strength by consuming more energy when being compressed (Table 3).

SEM-EDAX

Metakaolin shows a layered structure after the thermal treatment of kaolinite clay. Metakaolin shows almost equal contribution of silica and alumina. The Si/Al ratio of metakaolin is about 1.0 from EDAX analysis. Micro silica shows crystal patterns which are mostly of quartz in the micrograph image with a major contribution of silica showing a bigger particle size. Nano silica is a heterogeneous microstructure with some small round-shaped particles. EDAX analysis has been done for all the feedstocks and was found to be a major contribution of Si in micro and nano form (Fig. 12).

SEM analysis of before-heat samples M, MS5 and MM5 shows gel patterns with embedded aluminium phosphate phases. The surface of the samples is mostly covered with gel substrates with elements Si, Al and P. The P content analysed by EDS plays a vital role as the additive in phosphate-based geopolymer increases the P content. EDX results revealed that % P content in M is 2.7, MS5 is 6.7

Table 3 Assignments for Raman spectra of phosphate geopolymers

Wavenumber cm^{-1}	Assignments
123–225 cm^{-1}	Si–O stretching vibration and SiO_2
238–350 cm^{-1}	Al–O deformation and Al–O–P bending
327, 730 and 818 cm^{-1}	Al contributions of AlO_6, Al–O bending, Al_2O_3 vibration, and $AlPO_4$
400 to 580 cm^{-1}	Si–O–T (T = Si, Al or P) symmetric stretching vibration, SiO_2, and $AlPO_4$
634–699 cm^{-1}	Quartz and Si–O–Si bending vibration
709–730 cm^{-1}	Al–O bending vibration and Al–O–P
736 to 745 cm^{-1}	SiO_2 phase
950–1200 cm^{-1}	Si–O–T (T = Si, Al or P) symmetric stretching vibration, SiO_2, and $AlPO_4$

and for the MM5 sample, it is 8.1. From this, it is clear the incorporation of P in the SAP gel in turn micro silica involvement in the reaction with phosphoric acid with higher proposition has been embedded in the surface. The Si/P and Al/P also seem to be lower in MM5 and MS5 compared to M (Khabbouchi et al. 2017; Mathivet et al. 2019). A closer look at SEM pictures clarified that the heat-treated samples show more crystalline phases than the unheated sample. $MM5^{800}$ has more crystal grains in the matrix due to micro silica addition; usually, the raw micro silica has more crystal phases. The thermal treatment gives rise to different shapes of the crystalline phases seen in all the geopolymeric samples and a denser structure with a more uniform bright colour of the crystals. The Si/P and Al/P ratio is found to be lower in all after-heat-treated samples. Si/P ratio was found to be 4.7 in M^{800} 3.3 in $MS5^{800}$ and 2.81 in $MM5^{800}$, and the Al/P ratio is said to be 4.54 in M^{800}, 3.9 in $MS5^{800}$ and 1.98 in $MM5^{800}$. The heated sample shows higher P content; the highest P content is seen in $MM5^{800}$ with 10.0 (Fig. 13).

MAS-NMR

Solid-state MAS-NMR spectral analysis of all nuclei ^{29}Si, ^{27}Al and ^{31}P MAS NMR is used to investigate structural changes occurring due to the addition of silicious compounds and their interaction at elevated temperatures. The notation used in the ^{29}Si study is conventional as $Q^a(nAl)$ where a is the total number of atoms and n is the number of aluminium atoms bonded to a central silicon. (Figure 14) For the ^{31}P study, the notation used is $Q^x(yAl)$ where x is the number of phosphorous atoms, whereas y is the number of aluminium atoms bonded to a central phosphorous.

(a) ^{29}Si nuclei

The ^{29}Si NMR spectra of phosphate geopolymer show various chemical environments with ^{29}Si present in a $Q^4(0, 1, 2, 3)$-type environment detected in the range − 96 to − 108 ppm. The MAS-NMR of metakaolin (MK), the chemical shift and corresponding nuclei environments are $Q^4(1Al)$ at − 102 ppm and $Q^4(3Al)$ at − 91.8 ppm. Spectrum of micro silica which is mainly quartz phase as deduced from the XRD pattern showing the signals of the chemical shift ranges from − 115 to − 110 ppm with $Q^4(0Al)$ that corresponded to quartz only and − 105 ppm with $Q^4(1Al)$. Upon reaction, the phosphate is absorbed in the silicate network identified from the broad peak of Si nuclei in all silicate derivatives. Particularly, the hydrated form of Q^3-type silicate is actually related to Si–O–P and Si–O–Al. It has been reported that the signal at a stronger field corresponded to a connection between $[SiO_4]$ and $[AlO_4]$ tetrahedral unit, but the weaker field signal is between $[PO_4]$ and $[SiO_4]$. The environment $Q^4(1Al)$ identified from the chemical shift at − 104 ppm, in M (Figure S1) and $Q^4(2Al)$ is detected at − 97 ppm and − 99 ppm in both the geopolymers at ambient temperature (Vanitha and Jeyalakshmi 2023). The chemical shift of this $Q^4(1Al)$ in the raw material metakaolin MK at −102 ppm has a shift to − 104 ppm after geopolymerization, M. At the same time, the most connected Si–O–Si bond in the $Q^4(0Al)$ present in all samples corresponds to quartz and silicic acid in the range of chemical shift from − 107 to − 111 ppm. The MS5 spectrum shows two peaks overlapping at − 102 and − 103 ppm, which can be attributed to $Q^4(1Al, 1P)$ and $Q^4(1Al)$ environments that were not significant in M. Furthermore, $Q^4(3Al)$ at − 90.46 ppm in M is slightly shifted upfield at − 95 ppm, showing the involvement of P coordination and ascribed to $Q^4(2Al,1P)$. They are more prominent in MM5 and $MM5^{800}$due to more quartz phases that were unreactive from micro silica additive (Celerier et al. 2019; Partschefeld et al. 2020).

(b) 27Al nuclei

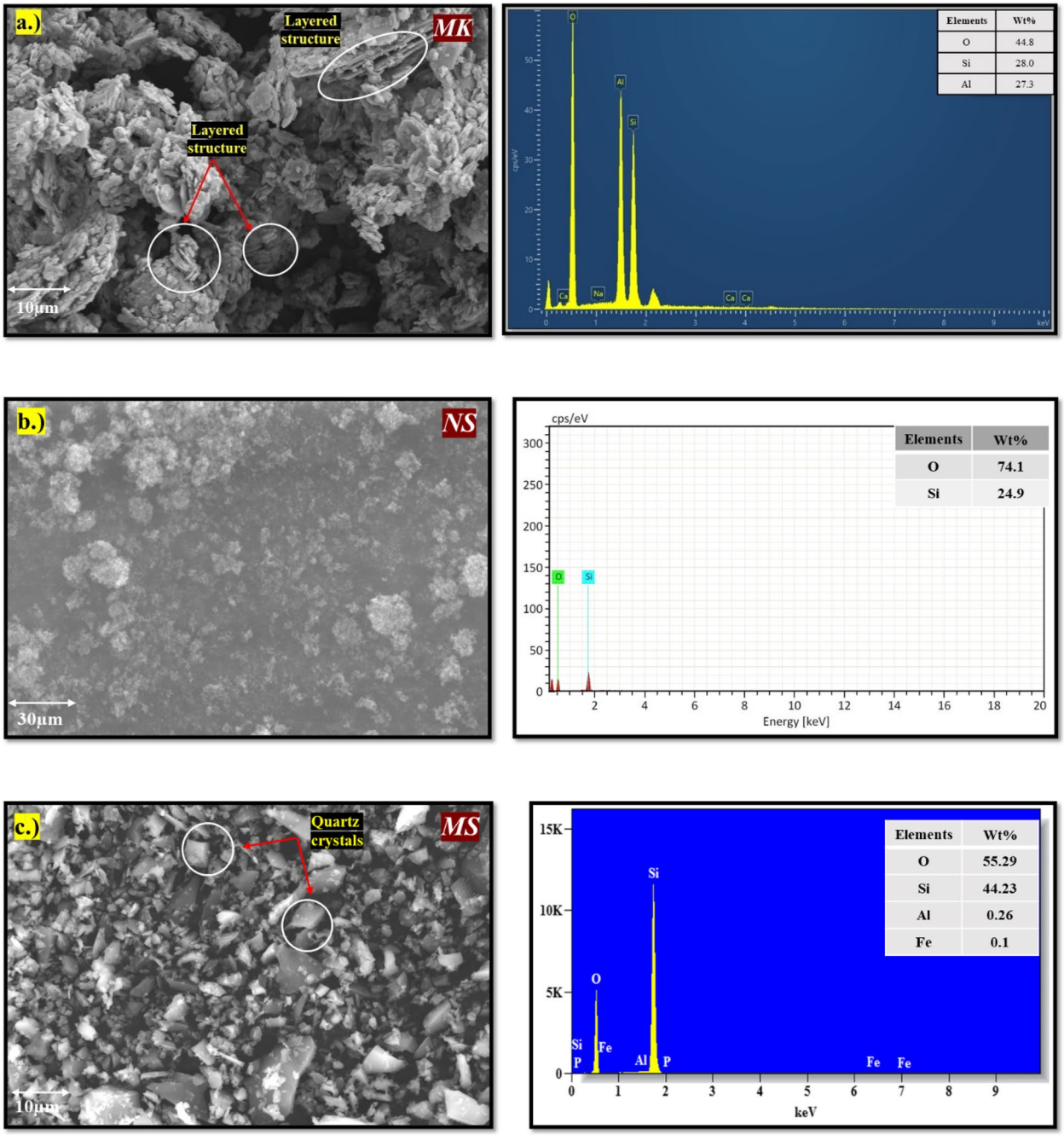

Fig. 12 SEM images of **a** metakaolin, **b** nano silica, and **c** micro silica

The ^{27}Al NMR shows a major change in the peak corresponding to the hexacoordinated Al coincides with the hydrated form of $AlPO_4$ and silico-aluminophosphate between the chemical shifts from 42 to 53 ppm. The Al in the raw metakaolin resolved the peak at 56 ppm and has tetra-coordination. The alumino-silicate peak present at − 8 to 3 ppm is corresponding to the hexacoordinated Al. The major penta-coordination is seen at 29.38 ppm, revealing the coordination of Al sites respectively. The tetrahedrally coordinated peaks, which are from alumina (aluminium hydroxide) precipitates and alumino-silicates, are generally observed in downfield shift, and thus, the observed peaks at 44 to 42 ppm in heat-treated samples of M^{800} (Figure S2), $MS5^{800}$ (Figure S2) and $MM5^{800}$confirmed the reaction of

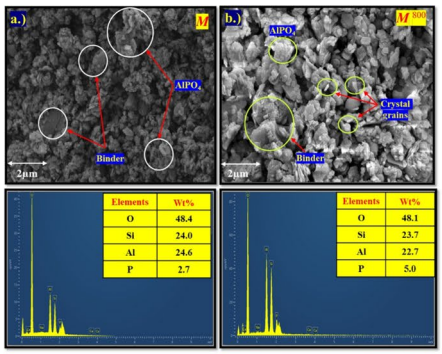

(a): SEM morphological image with elemental analysis of samples (a) M and (b) M^{800}

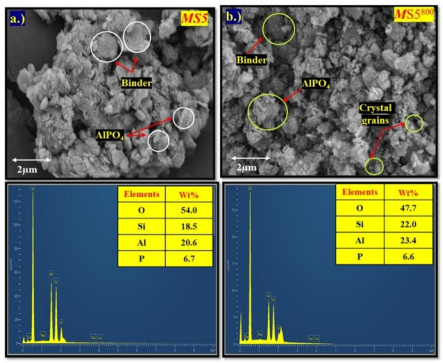

(b): SEM morphological image with elemental analysis of samples (a) MS5 and (b) $MS5^{800}$

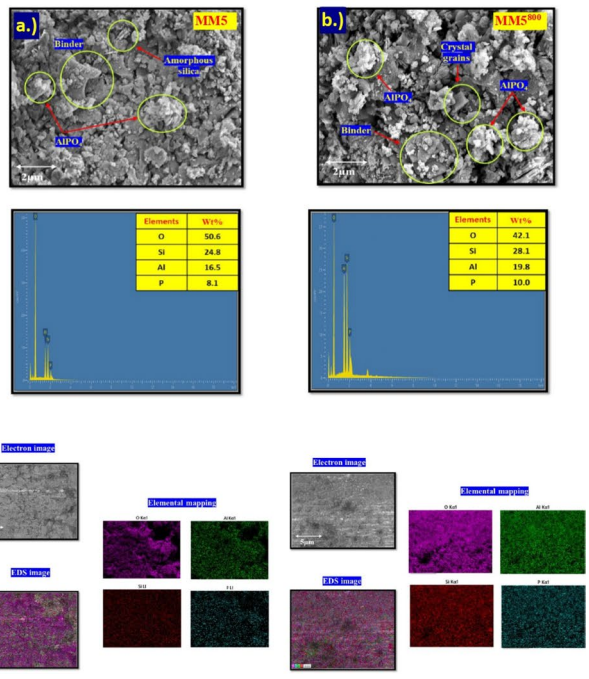

(c): SEM morphological image with elemental analysis and mapping of sample MM5 and $MM5^{800}$

Fig. 13 **a** SEM morphological image with elemental analysis of samples **a** M and **b** M^{800}. **b** SEM morphological image with elemental analysis of samples **a** MS5 and **b** $MS5^{800}$. **c** SEM morphological image with elemental analysis and mapping of sample MM5 and MM5.^{800}

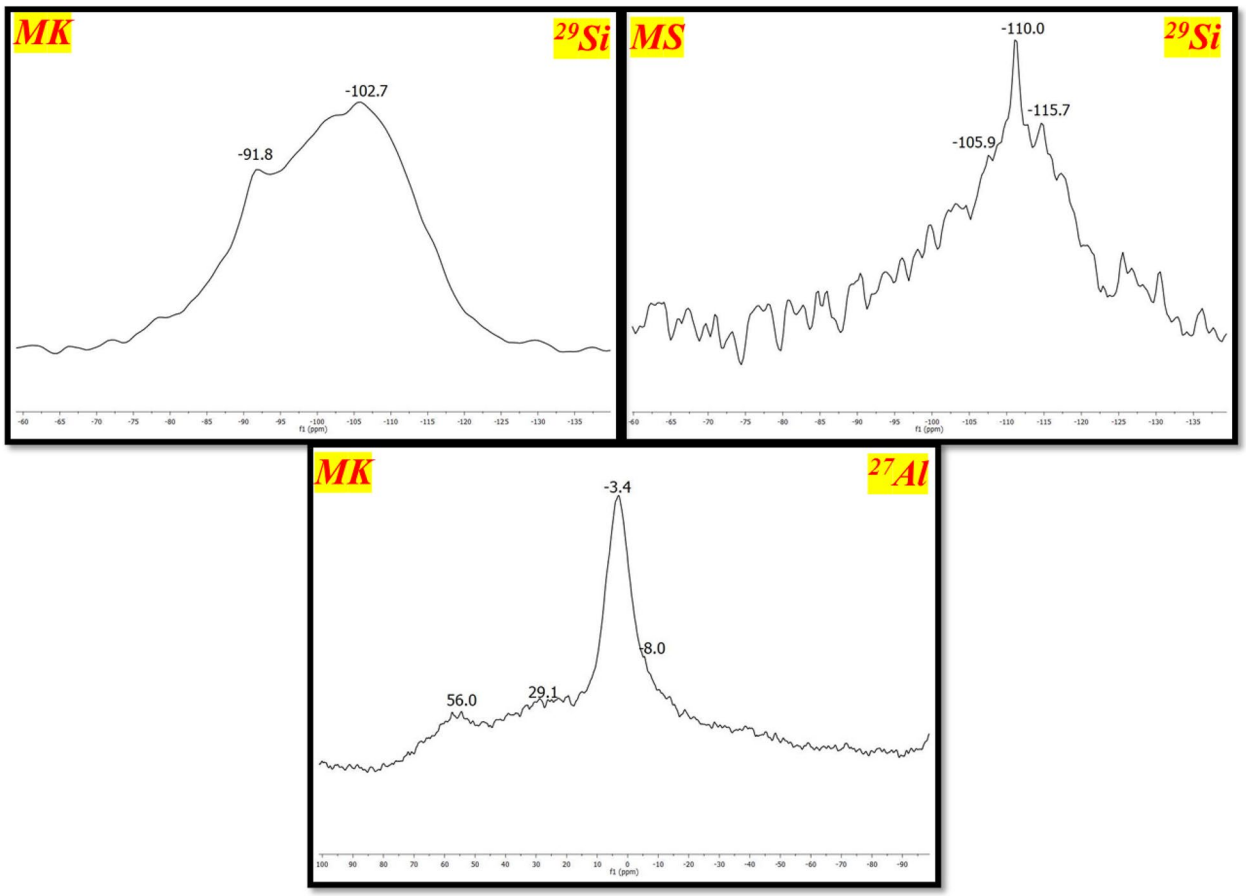

Fig. 14 ^{29}Si and ^{27}Al MAS-NMR of raw materials

cross-condensation of Al and P (Celerier et al. 2019; Vanitha and Jeyalakshmi 2023). Apparently, this peak is only from tetrahedral Al–O–P base phases. Thus, thermal treatment led to the crystalline lattice, which is mainly formed from Q^4(0Al) of silica and tetrahedral aluminium atoms. The nonobservance of the peak at around − 10 to − 20 ppm indicated that there is no residual Al of metakaolin in the hexacoordinated structure. On the other hand, a peak present at − 2 to − 8 ppm correspond to the hexacoordinated Al as $Al(PO_2)_4(OH)_2$cannot be omitted (Vanitha et al. 2022; Partschefeld et al. 2020). From the results, one can say the addition of the small amount of micro silica improved the oxo-bridged coordination of Al and P with more hydrated compounds.

(c) ^{31}p nuclei

The analysis of the P NMR signal was carried out to have a clear picture of the changes in the P environment. ^{31}P MAS-NMR spectra resonate at − 12 ± 2 and − 19 ppm attributed to the P–O–P linkages present in Al–O–P–O and Al–O–P–OH network. At elevated temperatures, the chemical shift values are shielded (P1 sites) at − 28 ± 2 and 33 ppm, which is identical in all heat-treated samples irrespective of the reactive mixture. The predominant peak in cured samples is polymerized phosphorous peak resonates at − 12 to − 14 ppm, and the deshielding direction (− 12 ± 2) ppm peak is from the layer phase of metakaolin geopolymer which is directly linked to a lower degree of P condensation or, in other words, polymerized phosphate aluminium network of P–O–Al unit with a small angle (Celerier et al. 2019; Vanitha and Jeyalakshmi 2023). But thermal-induced crystallization of various aluminophosphate phases moves this P environment to a more shielded direction. It seems that the P local environment developed a nonequivalent P site upon crystallization, which corresponds to the broad tetrahedral resonance of Al sites. Various signals observed for different nuclei and the corresponding assignments are given in Fig.15 (c).

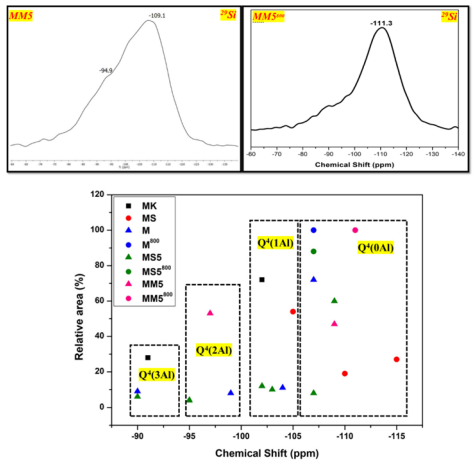

(a) : ^{29}Si NMR spectra of MM5 and MM5^{800} and relative area of all samples with different contributions with respect to their chemical shifts

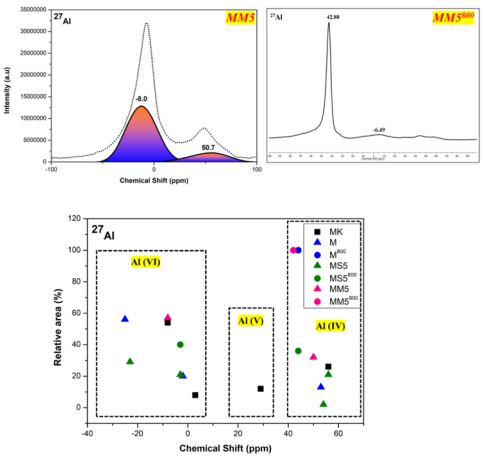

(b) : ^{27}Al NMR spectra of MM5 and MM5^{800} and relative area of all samples with different contributions with respect to their chemical shifts

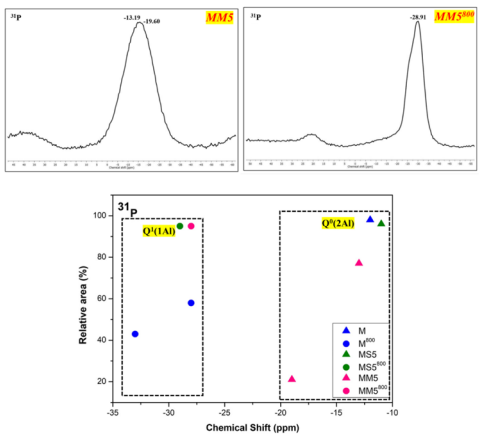

(c) : ^{31}P NMR spectra of MM5 and MM5^{800} and relative area of all samples with different contributions with respect to their chemical shifts

◀ **Fig. 15** **a** ^{29}Si NMR spectra of MM5 and MM5^{800} and relative area of all samples with different contributions with respect to their chemical shifts. **b** ^{27}Al NMR spectra of MM5 and MM5^{800} and relative area of all samples with different contributions with respect to their chemical shifts. **c** ^{31}P NMR spectra of MM5 and MM5^{800} and relative area of all samples with different contributions with respect to their chemical shifts

X-ray photoelectron spectral analysis

The XPS analysis of geopolymers is quite difficult due to their nonuniform surface charges and the broadened photoelectron lines. It becomes even more difficult when more phases are generated on thermal treatment. However, XPS is a very convenient method of analysis to understand the chemical state of the elements as the surface binding energy can be related to the electronic environment of the typical element. Here, this technique is used to follow the chemical reaction of phosphoric acid in the presence of reactive additives and the changes in the products because of exposure to elevated temperature. Since limited literature is available on metakaolin phosphosilicates under thermal treatment, a discussion of the assignment of the initial polymerized network and the dehydrated products established from XRD and NMR data is done here. The main polymerized network made up of the phosphate group is in itself complex due to the presence of silicate as well as aluminate species in the same region. Therefore, to explain the binding energy of the different elemental components such as hydrated silica, vitreous silica, aluminophosphates and silico-aluminophosphate network, the position and intensity of Si, Al, O, P and Ca atoms are assessed (Kanuchova et al. 2014; Duxson et al. 2006).

The general observation is % of aluminium, and silicon tends to decrease in geopolymers as ions are involved in the geopolymerization reaction. Al 2p peak intensity gradually decreases upon geopolymerization, and that of P increases, because of the partial substitution of Si–O–Si by Si–O–P bonds. This is nothing but an inclusion of a PO_4 unit in the network suggesting the formation of long-chain Si–O–P–O–Si of poly (phospho-siloxo) units. The above-mentioned reactive bonds influence is established from our NMR results. The survey line spectra graphs are depicted in Fig. 16a and b.

Linear thermal expansion

Thermal shrinkage is one of the factors that can determine the volumetric stability at all temperatures and measure the volume decrease of the binder in the absence of external factors. Thermal shrinkage is increased by low heating rates up to the point of structural densification in all geopolymers, while the inverse is true from the onset of densification. The dilatometry curves show the

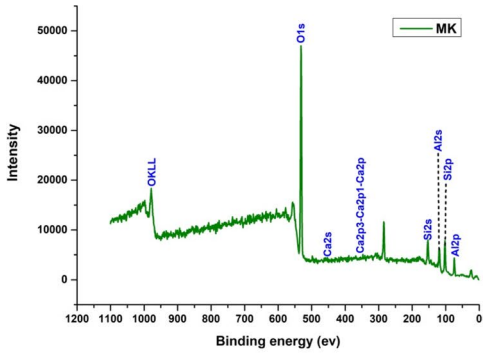

(a) : XPS survey line spectra of MK

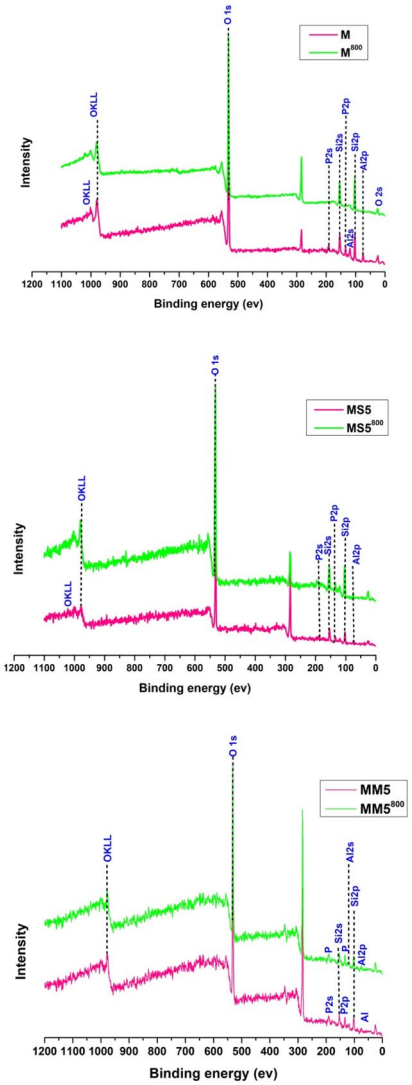

(b) : XPS survey line spectra of M,MS5 and MM5 before and after heat

Fig. 16 **a** XPS survey line spectra of MK. **b** XPS survey line spectra of M, MS5, and MM5 before and after heat

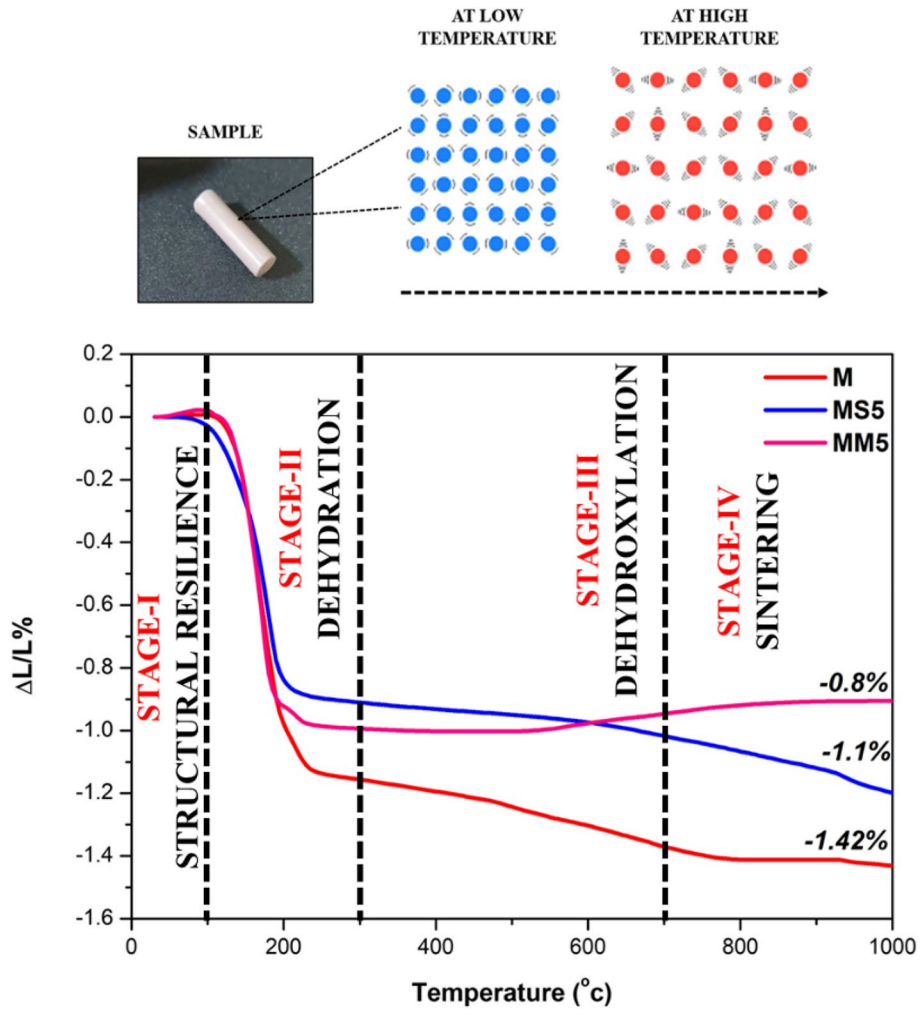

Fig. 17 Thermal expansion of phosphate geopolymer samples M, MS5, and MM5

thermal linear shrinkage patterns in geopolymer samples which are measured up to 1000 °C are depicted in Fig. 17. All specimens exhibited four thermal shrinkage stages, namely (stage I) structural resilience, (stage II) dehydration, (stage III) dehydroxylation and (stage IV) sintering stage.

The first shrinkage occurs between 25 and 100 °C and reaches its maximum at 110–140 °C, and the shrinkage was produced in the range of about − 1.1% for geopolymer specimen M. It is related to physically bound water; this is also identified in the thermogram of M. The increase in temperature after the first shrinkage correlates with the extent of cracks observed on the surface of specimens normally above 100 °C which corresponds to the onset temperature for the evaporation of water. The second shrinkage begins at 100 °C and ends before 400 °C display the same shrinkage rate of − 1.1%. The slow and constant rate of shrinkage in the temperature range between 300 and 580 °C is due to the physical contraction of the gel. The geopolymeric reaction in mechanistic steps involved the release of water molecules through dehydroxylation and polycondensation of oligomeric silanol or aluminol to form a network Si–O–T tetrahedral linkage.

The third stage is linked to the physical contraction of phosphate-based geopolymer, while looking at the T–OH (T = Si, Al or P) product from the polycondensation process underwent dehydroxylation process which can be extended above the temperature 300 to 900 °C. In the temperature region 300–900 °C, the shrinkage rate is about − 1.4%. The final stage above 900 °C has significant thermal shrinkage with − 1.4% in sample M, which was due to both skeletal densification and the elimination of large pores by viscous sintering. In viscous flow sintering, atomic movement occurs by a cooperative motion mechanism rather than individual diffusion, and this has been studied. The same behaviour has been evidenced by the heavy mass loss in TGA/DTA.

Due to physically bonded water, the shrinkage at 200 °C was determined to be − 0.8% in MS5 and − 0.7% in MM5 which is significantly less than the quartz phase in MM5 which is more stable at high temperatures, and increases in temperature do not significantly affect the matrix shrinkage rate as it exhibits very little change after 600 °C, with a shrinkage rate of roughly − 0.8%. The control sample M exhibits the greatest value of − 1.4% at 1000 °C; when additive MS5 exhibits − 1.1% and MM5 − 0.8%, the results are even lower. Thus, thermal shrinkage values are much lower than metakaolin alkali-activated geopolymer as reported in the range of 1.15 to 1.65 by P. Duxson et al. (2006).

These facts are derived from thermal analysis where the primary cause of mass loss and physical contraction is the gradual dehydration and dehydroxylation of bound water molecules present in the phosphate geopolymer samples. The hydroxyl group dislocation limits the physical rearrangement in the mid-temperature range, and the gels of the poly-phospho-siloxo network formed between the hydroxyl groups of silanol and aluminol undergo a slight physical contraction. Otherwise, the bulk expansion of the sample is restricted by the condensation of Si and Al linkages in a tetrahedral geometry. Because of softening and sintering, the matrix densifies, and the onset temperature rises sharply at high temperatures (Liu et al. 2012; Djobo et al. 2019). Comparing the control specimens, silica-enriched phases in MM5 were found to be more thermally stable with low shrinkage.

Thermal conductivity

The ability of the metakaolin phosphate geopolymer with nano and micro geopolymer composites to conduct heat was determined by employing their thermal conductivity (W/mK). It was found that when the temperature increased from room temperature to 200 °C, the produced geopolymeric paste samples' thermal conductivity values were minimized (the thermal conductivity at ambient temperature or "k" value). The fine capillary pores present in the phosphate geopolymer matrix are responsible for transporting the moisture content through the matrix, which increases the conductivity. Control sample M has 3.8 W/mK at 40 °C at first, but as the temperature rises, it steadily drops to 0.6 W/mK at 200 °C. The thermal conductivity value in M is caused by chemically confined water, which creates a continuous gel structure for heat transport. The convoluted pathway for thermal gradient flow was supplied by the amorphous and interconnected poly-phospho-siloxo network created by the geopolymerization process (Gualtieri et al. 2015). At room temperature, the geopolymer sample showed 3.4 W/mK for sample MS5 which is slightly less in MM5 with 3.1 W/mK. At 200 °C, geopolymer samples supplemented with nano and micro additives exhibit 0.10–0.61 W/mK. It is evident from this that the heat transfer was hindered by greater gel structure. It was observed that there is a decrease in thermal conductivity with the addition of micro- and nano-sized particles as compared to control samples. This can be reason out to their high surface to volume ratios (Chari et al. 2013). The smaller grains of nano silica will pack the particles closer, forming a more homogenous specimen, thereby increasing in conductivity. At the same time, the presence of void spaces, which are created in the sample, is completely dependent on the particle size that led MS5 sample with lower thermal conductivity (Chari et al. 2013). The present work is applicable and suitable for thermal insulators (Table 4).

Effect of nano and micro form of silica in metakaolin phosphate geopolymer: chemical and thermomechanical transformation reaction

When samples M, MS5 and MM5 were under thermal treatment, the chemical transformation was deduced from XRD, and they were more of silica phases due to the removal of OH groups from dehydration followed by dehydroxylation reaction. So, finally, the Si–O–P networks with SiO_2 are the predominant phases observed. The same coincided with the identified NMR signals corresponding to $Q^4(0Al)$ for heat-treated samples under the peak maxima at − 107 ppm. This broad peak was attributable to the oxides of silica. The peak resonating at − 111 ppm in MM^{800} is attributed to the crystalline broad peak masks of the quartz peak at − 109 ppm. Therefore, the arrangements of aluminosilicate-layered structure in all the samples led to the most stable silica form after dehydration. The test results of the nanoindentation combined with microscope image analysis supported an evaluation of the potential of the new

Table 4 Thermal conductivity values for samples M, MS5 and MM5 from 40 to 200 °C

Temperature (°C)	Sample ID		
	M	MS5	MM5
40	3.88	3.44	3.10
60	2.12	1.68	1.65
80	1.46	1.24	1.04
100	1.19	0.64	0.49
120	0.90	0.28	0.19
140	0.80	0.14	0.16
160	0.66	0.10	0.11
180	0.64	0.10	0.10
200	0.61	0.10	0.10

glass compositions to be utilized for building engineering purposes. Crystalline phase berlinite and SAP gel are responsible for strength attainment in bulk property, and additive reinforced sample shows higher strength compared to M. This trend is similar in the nanoindentation method by their increasing E and H values. Compared with M, micro silica-reinforced samples show higher hardness and elasticity values with a high denser gel phase with some Al- and Si-rich partially active phase, while MS5 has both high- and low-dense gel due to the amorphous form of silica in the sample. Proving the formation of geopolymeric network like Al–O–P, Si–O–P, Si–O–Si, $AlPO_4$ and SiO_2 phases which are identified in the Raman frequency ranges between 900 and 1500 cm^{-1} in geopolymer samples at ambient and heat treated. The below scheme gives a probable explanation for the chemical and thermal transformation reaction which is depicted in Fig. 18.

Conclusion

It can be observed in the current work that the thermal properties of geopolymeric material were derived from the metakaolin phosphoric acid route and are greatly influenced by the addition of a small amount of nano and micro silica. The nanoscale mechanical performance investigated in this study coincides with the bulk properties. To the best of our knowledge, these nanoindentation study results were reported for the first time in the metakaolin phosphate geopolymer matrix. From the loading curves, the gel phase was identified through

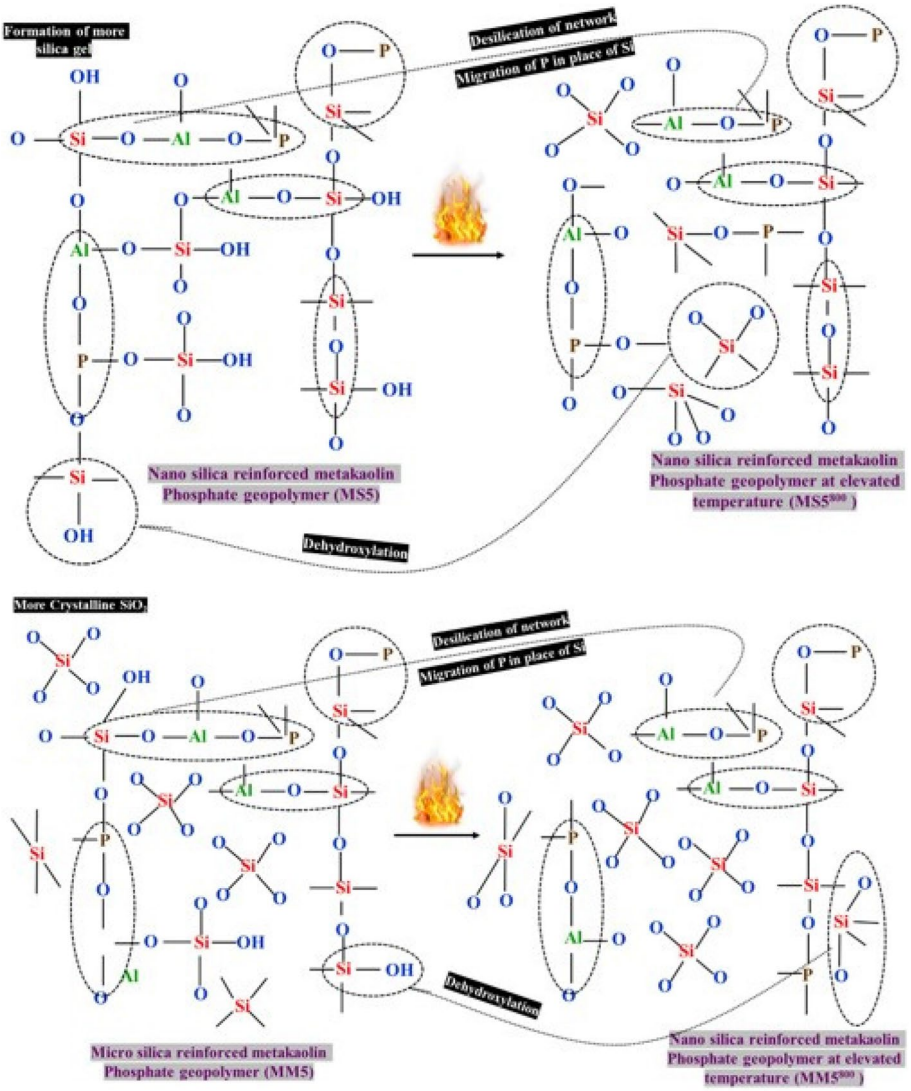

Fig. 18 Network changes upon thermal treatment

a hardness value of 0.9 to 1.3 GPa, and elasticity value ranges between 31.9 and 43.7 GPa which are from generally heterogeneous phases of the phosphate geopolymer matrix. The addition of nano micro silica improved the microhardness of the network of metakaolin at a small dose of 5%. The physical evolution of materials during heating is a critical factor in determining their suitability and performance for applications ranging from construction to refractories and adhesives. Therefore, the physical evolution of the phosphate-excited metakaolin was investigated, and the addition of the silica was found to reduce the shrinkage effectively.

The microstructural changes before and after heat treatment were investigated with various analytical techniques, and the following are the salient features identified:

✔ The readily active Si from nano and micro silica forms Si-rich phosphate gel in the metakaolin phosphate geopolymer which enhances the matrix with silico-aluminophosphate network. The improved thermal performance and structural resilience are thought to be due to the increased strength of the Al–O–P bond in ambient temperature and more silica refractory phases in the heat-treated samples.
✔ In XRD, the conversion of berlinite to phosphocristobalite and tridymite identified in the heat-treated samples that they manifest themselves for gel softening at high temperatures
✔ The infrared spectra of geopolymer samples show that the product has a polymeric Si–O–Al–O–P structure. The incorporation of nano and micro additives does not produce any new compound.
✔ Al–O–P, Si–O–P, Si–O–Si, $AlPO_4$ and SiO_2 phases are identified in the Raman frequency range between 900 and 1500 cm^{-1} range in both M and MM at ambient and heat treated.
✔ SEM images are clarified with more crystal grains with aluminium phosphate and SiO_2 phases in heat-treated samples of MM5.
✔ ^{29}Si NMR signals corresponding to $Q^4(0Al)$ in both the samples with Si–O–P networks and SiO_2 are the predominant phases observed. Hexacoordinated Al with the hydrated form of $AlPO_4$ and silico-aluminophosphate are deduced from the chemical shifts range from 42 to 53 ppm of ^{27}Al NMR.
✔ Thermally stable bonds of Al–O–P and Si–O are established from the XPS binding energy lines.
✔ Thermal analysis and thermal shrinkages of the specimens can be categorized in the regions of structural resilience, dehydration, dehydroxylation, and sintering. The reduction of the crack, pores and smooth topography surface in SEM of the M, MS5 and MM5 samples at room temperature is consistently attributed to a high degree of gel organization during the reaction.
✔ Microstructural analysis of heat-treated samples showed the densification of the matrix by the thermally produced silica phases at elevated temperatures in addition to the reduction of the porosity.
✔ The extent of thermal shrinkage in the current work observed a decrease in order from control M (–1.4%), MS5 (–1.1) to MM5 (–0.8%). This typical trend is observed in thermal conductivity also.
✔ In DTA, the temperature span of the endotherm from ambient to 450 °C at control samples attributed to loss of free water molecules from pores, and this span decreased in MS5 and MM5 samples with reduced mass loss.

By considering all the test results from various analytical techniques investigated, it is inferred that chemical additives, nano and micro sized, silica influence the phosphoric acid attack on metakaolin. After firing, the generation of Si–O–linkages induced the crystallization of different silica phases and enhanced the thermal stability. Thus, the use of a small addition of micro silica is an interesting route to prepare phospo geopolymers with improved performance and thermal resistance properties.

Abbreviations

HT	High temperature
LT	Low temperature
GPa	Gigapascal
MPa	Megapascal
E	Elasticity
H	Hardness

Supplementary Information

The online version contains supplementary material available at https://doi.org/10.1186/s40712-024-00176-6.

Supplementary Material 1: Figure S1: ^{29}Si NMR spectra of M, MS5, M^{800} and $MS5^{800}$. Figure S2: ^{27}Al NMR spectra of M, MS5, M^{800} and $MS5^{800}$. Figure S3: ^{31}P NMR spectra of M, MS5, M^{800} and $MS5^{800}$.

Acknowledgements
The authors greatly acknowledge the utilization of facilities provided by NRC, the Department of Chemistry and the SRM Institute of Science and Technology. The authors acknowledge technical assistants, the Strength of Material Laboratory, the Department of Mechanical Engineering and the SRM Institute of Science and Technology for the compression testing facility. The authors would like to thank and acknowledge Kiran Mangalampalli, Nanoindentation Laboratory, the Department of Physics and Nanotechnology, SRM Institute of Science and Technology

Authors' contributions
NV, investigation, methodology, data curation and writing of the original draft. RT and MM, methodology and data curation. SNM, investigation and data curation. MK, conceptualization, formal analysis and resource. RJ,

conceptualization, formal analysis, resource, funding, review and editing and supervision.

Funding
This work was supported by the Department of Science and Technology, Government of India (GOI), under the grant DST/TDT/WMT/2017 14/03/18, GOI.

Availability of data and materials
The data sets used and/or analysed during the current study are available from the corresponding author on reasonable request.

Declarations

Competing interests
The authors declare that they have no competing interests.

Author details
[1]Department of Chemistry, College of Engineering and Technology, SRM Institute of Science and Technology, Tamil Nadu, Kattankulathur 603203, India. [2]Department of Physics and Nanotechnology, College of Engineering and Technology, SRM Institute of Science and Technology, Tamil Nadu, Kattankulathur 603203, India. [3]Department of Interdisciplinary Institute of Indian System of Medicine, SRM Institute of Science and Technology, Tamil Nadu, Kattankulathur 603203, India.

Received: 23 May 2024 Accepted: 2 September 2024
Published online: 26 September 2024

References

Abdel-Kader A, Higazy AA, Elkholy MM (1991) "Compositional dependence of infrared absorption spectra studies for TeO_2-P_2O_5 and TeO_2-P_2O_5-Bi_2O_3 glasses,." Journal of Materials Science Materials in Electronics 2(3):157–163

Allahdin O, Wartel M, Tricot G (2016) "Hydroxylation and dealumination of a metakaolinite-rich brick under acid conditions, and their influences on metal adsorption: one- and two-dimensional (^{1}H, ^{27}Al, ^{23}Na, ^{29}Si) MAS NMR, and FTIR studies,." Microporous & Mesoporous Materials 226:360–368

Autef A, Joussein E, Gasgnier G, Rossignol S, (2012), Role of the silica source on the geopolymerization rate, J. Non. Cryst. Solids. 358,2886–2893, https://doi.org/10.1016/J.JNONCRYSOL.2012.07.015

Bai C, Conte A, Colombo P (2017) Open-cell phosphate-based geopolymer foams by frothing. Mater Lett 188:379–382

Bezerra BP, Morelli MR, Luz AP (2023) Effect of reactive silica sources on the properties of Na-metakaolin-based geopolymer binder. Constr Build Mater 364:129989

Cao D, Su D, Lu B, Yang Y (2005) Synthesis and structure characterisation of geopolymeric material based on metakaolinite and phosphoric acid. Journal of the Chinese Ceramic Society, Guisuanyan Xuebao 33(11):1385–1389

Celerier H, Jouin J, Tessier-Doyen N, Rossignol S (2018) Influence of various metakaolin raw materials on the water and fire resistance of geopolymers prepared in phosphoric acid. J Non-Cryst Solids. https://doi.org/10.1016/j.jnoncrysol.2018.09

Celerier H, Jouin J, Gharzouni A, Mathivet V, Sobrados I, Tessier-Doyen N, Rossignol S (2019) Relation between working properties and structural properties from ^{27}Al, ^{29}Si and ^{31}P NMR and XRD of acid-based geopolymers from 25 to 1000° C. Mater Chem Phys 228:293–302. https://doi.org/10.1016/j.matchemphys.2019.02.049

Chari, V.D., Sharma, D.V.S.G.K., Prasad, P.S.R. et al. (2013) Dependence of thermal conductivity in micro to nano silica. bull mater sci 36, 517–520 https://doi.org/10.1007/s12034-013-0519-3

Davidovits Joseph (2008) Geopolymer. Chemistry and applications, Institute Geopolymere, Saint-Quentin, France

Deb PS, Khan MNN, Sarker PK, Barbhuiya S (2022) Nanomechanical characterization of ambient-cured fly ash geopolymers containing nanosilica. Journal of Sustainable Cement-Based Materials 11(3):164–174

Demirel B, Kelestemur O (2010) Effect of elevated temperature on the mechanical properties of concrete produced with finely ground pumice and silica fume. Fire Saf J 45:385–391

Díaz-Pérez M, Grima L, Moshtaghioun BM, Pena JI (2021) CaO–MgO–SiO_2–P_2O_5-based multiphase bio-ceramics fabricated by directional solidification: microstructure features and in vitro bioactivity studies. Ceram Int 47(12):17041–17048

Djobo JNY, Elimbi A, Stephan D (2019) Phase and dimensional stability of volcanic ash-based phosphate geopolymers at elevated temperatures. PROCEEDINGS ICSBM VOLUME 3:80

Douiri H, Louati S, Baklouti S, Arous M, Fakhfakh Z (2014) Structural, thermal and dielectric properties of phosphoric acid-based geopolymers with different amounts of H3PO4. Mater Lett 116:9–12. https://doi.org/10.1016/j.matlet.2013.10.075

Dutta D, Thokchom S, Ghosh P, Ghosh S (2010) Effect of silica fume additions on porosity of fly ash geopolymers. ARPN J Eng Appl Sci 5:74–79

Duxson P, Lukey GC, van Deventer JS (2006) Thermal evolution of metakaolin geopolymers: part 1–physical evolution. J Non-Cryst Solids 352(52–54):5541–5555

Ettoumi H, Ben Ahmed A, Suñol JJ, Toumi M (2023) Effect of CuO added to aluminosilicate phosphate geopolymer, structure and optical properties analysis. Journal of Inorganic and Organometallic Polymers and Materials 33(12):1–9

Farahani A, Taghaddos H, Shekarchi M (2015) Prediction of long-term chloride diffusion in silica fume concrete in a marine environment. Cem Concr Compos 59:10–17

Gowda R, Narendra H, Rangappa D, Prabhakar R (2017) Effect of nano-alumina on workability, compressive strength and residual strength at elevated temperature of cement mortar. Mater Today Proc 4:12152–12156. https://doi.org/10.1016/j.matpr.2017.09.144

Gualtieri ML, Romagnoli M, Gualtieri AF (2015) Preparation of phosphoric acid-based geopolymer foams using limestone as pore forming agent – thermal properties by in situ XRPD and Rietveld refinements. J Eur Ceram Soc 35:3167–3178. https://doi.org/10.1016/j.jeurceramsoc.2015.04.030

He Z, Qian C, Zhang Y, Zhao F, Hu Y (2013) Nanoindentation characteristics of cement with different mineral admixtures. SCIENCE CHINA Technol Sci 56(5):1119–1123

He Y, Liu L, He L, Cui X (2016) Characterization of chemosynthetic H_3PO_4–Al_2O_3–$2SiO_2$ geopolymers. Ceram Int 42(9):10908–10912. https://doi.org/10.1016/j.ceramint.2016.03.224

Heikal M, Ismail MN, Ibrahim NS (2015) Physico-mechanical, microstructure characteristics and fire resistance of cement pastes containing Al_2O_3 nano-particles. Constr Build Mater 91:232–242. https://doi.org/10.1016/j.conbuildmat.2015.05.036

Hu C, Li Z, Gao Y, Han Y, Zhang Y (2014) Investigation on microstructures of cementitious composites incorporating slag. Adv Cem Res 26(4):222–232

Hui Lin, Hui Liu, Yue Li, Xiangming Kong,Properties and reaction mechanism of phosphoric acid activated metakaolin geopolymer at varied curing temperatures. Cement and Concrete Research, 106425, (2021). https://doi.org/10.1016/j.cemconres.2021.106425

Izci E (2014) Structural and dielectric properties of acid activated metakaolinite and kaolinite. 11th International GeoRaman Conference (Vol. 1783, p. 5097)

Jouin J, Celerier H, Ouamara L, Tessier-Doyen N, Rossignol S (2021) Study of the formation of acid-based geopolymer networks and their resistance to water by time/temperature treatments. J Am Ceram Soc 104(10):5445–5456. https://doi.org/10.1111/jace.17929

Kanuchova M, Kozakova L, Drabova M, Sisol M, Estokova A, Kanuch J, Skvarla J (2014) Monitoring and characterization of creation of geopolymers prepared from fly ash and metakaolin by X-ray photoelectron spectroscopy method. Environ Prog Sustainable Energy 34(3):841–849

Katsiki A (2019) Aluminosilicate phosphate cements–a critical review. Adv Appl Ceram 118(5):274–286

Katsiki A, Hertel T, Tysmans T, Pontikes Y, Rahier H (2019) Metakaolinite phosphate cementitious matrix: inorganic polymer obtained by acidic activation. Materials 12(3):442

Keeley PM, Rowson NA, Johnson TP, Deegan DE (2017) The effect of the extent of polymerisation of a slag structure on the strength of alkali-activated slag binders. Int J Miner Process 164:37–44

Khabbouchi M, Hosni K, Mezni M, Zanelli C, Doggy M, Dondi M, Srasra E (2017) Interaction of metakaolin-phosphoric acid and their structural evolution

at high temperature. Appl Clay Sci 146:510–516. https://doi.org/10.1016/j.clay.2017.07.006
Khabbouchi M, Hosni K, Mezni M, Srasra E (2018) Simplified synthesis of silicophosphate materials using an activated metakaolin as a natural source of active silica. Appl Clay Sci 158:169–176. https://doi.org/10.1016/j.clay.2018.03.027
Kong D, Du X, Wei S, Zhang H, Yang Y, Shah SP (2012) Influence of nano-silica agglomeration on microstructure and properties of the hardened cement-based materials. Constr Build Mater 37:707–715
Krishna Rao A, Rupesh Kumar D, Comparative study on the behaviour of GPC using silica fume and fly ash with GGBS exposed to elevated temperature and ambient curing conditions, (2020) Mater. Today Proc 27:1833–1837
Lee H, Vimonsatit V, Chindaprasirt P (2016) Mechanical and micromechanical properties of alkali activated fly-ash cement based on nano-indentation. Constr Build Mater 107:95–102
Lilkov V, Rostovsky I, Petrov O, Tzvetanova Y, Savov P (2014) Long term study of hardened cement pastes containing silica fume and fly ash. Constr Build Mater 60:48–56
Liu LP, Cui XM, He Y, Liu SD, Gong SY (2012) The phase evolution of phosphoric acid-based geopolymers at elevated temperatures. Mater Lett 66(1):10–12. https://doi.org/10.1016/j.matlet.2011.08.043
Luo Z, Li W, Gan Y, He X, Castel A, Sheng D (2021) Nanoindentation on micromechanical properties and microstructure of geopolymer with nano-SiO_2 and nano-TiO_2. Cement Concr Compos 117:103883
Majdoubi H, Haddaji Y, Mansouri S, Alaoui D, Tamraoui Y, Semlal N, Hannache H (2021) Thermal, mechanical and microstructural properties of acidic geopolymer based on Moroccan kaolinitic clay. Journal of Building Engineering 35:102078. https://doi.org/10.1016/j.jobe.2020.102078
Mathivet V, Jouin J, Gharzouni A, Sobrados I, Celerier H, Rossignol S, Parlier M (2019) Acid-based geopolymers: understanding of the structural evolutions during consolidation and after thermal treatments. J Non-Cryst Solids 512:90–97. https://doi.org/10.1016/j.jnoncrysol.2019.02.025
Mierzwiński D, Łach M, Hebda M, Walter J, Szechyńska-Hebda M, Mikuła J (2019) Thermal phenomena of alkali-activated metakaolin studied with a negative temperature coefficient system. J Therm Anal Calorim 138:4167–4175
Miller M, Bobko C, Vandamme M, Ulm F-J (2008) Surface roughness criteria for cement paste nanoindentation. Cem Concr Res 38(4):467–476
Mondal P, Shah SP, Marks LD, Gaitero JJ (2010) Comparative study of the effects of microsilica and nanosilica in concrete. Transp Res Rec 2141(1):6–9
Morales M, Formosa J, Xuriguera E, Niubo M, Segarra M, Chimenos JM (2015) Elastic modulus of a chemically bonded phosphate ceramic formulated with low-grade magnesium oxide determined by nanoindentation. Ceram Int 41(9):12137–12146
Mustakim SM, Das SK, Mishra J, Aftab A, Alomayri TS, Assaedi HS, Kaze CR (2021) Improvement in fresh, mechanical and microstructural properties of fly ash-blast furnace slag based geopolymer concrete by addition of nano and micro silica. SILICON 13:2415–2428
Němeček J, Šmilauer V, Kopecký L (2009) Characterization of alkali-activated fly-ash by nanoindentation. Nanotechnology in Construction 3:337–343
Němeček J, Šmilauer V, Kopecký L (2011) Nanoindentation characteristics of alkali-activated aluminosilicate materials. Cement Concr Compos 33(2):163–170
Nobouassia Bewa C, Tchakouté HK, Fotio D, Rüscher CH, Kamseu E, Leonelli C (2018) Water resistance and thermal behavior of metakaolin-phosphate-based geopolymer cements. Journal of Asian Ceramic Societies 6(3):271–283
Nochaiya T, Wongkeo W, Chaipanich A (2010) Utilization of fly ash with silica fume and properties of portland cement–fly ash-silica fume concrete. Fuel 89(3):768–774. https://doi.org/10.1016/j.fuel.2009.10.003
Nuruzzaman M, Sarker PK, Shaikh FUA (2023) The interfacial transition zone microstructure of ground ferronickel slag incorporated self-compacting concrete investigated by nanoindentation. Journal of Building Engineering 71:106437
Okoye FN, Durgaprasad J, Singh NB (2016) Effect of silica fume on the mechanical properties of fly ash based-geopolymer concrete. Ceram Int 42(2):3000–3006
Oliver WC, Pharr GM (2004) Measurement of hardness and elastic modulus by instrumented indentation: advances in understanding and refinements to methodology. J Mater Res 19(1):3–20
Partschefeld, S., Wiegand, T., Bellmann, F., &Osburg, A,Formation of geopolymers using sodium silicate solution and aluminum orthophosphate. (2020), Materials, 13(18), 4202, https://doi.org/10.3390/ma13184202
Partschefeld S, Wiegand T, Bellmann F, Osburg A (2020) "Formation of geopolymers using sodium silicate solution and aluminum orthophosphate,." Materials 13(18):4202
Perera DS, Hanna JV, Davis J, Blackford MG, Latella BA, Sasaki Y, Vance ER (2008) Relative strengths of phosphoric acid-reacted and alkali-reacted metakaolin materials. J Mater Sci 43(19):6562–6566. https://doi.org/10.1007/s10853-008-2913-6
Pharr GM, Bolshakov A (2002) Understanding nanoindentation unloading curves. J Mater Res 17(10):2660–2671
Ping Duan AB, Chunjie Yan AB, Wei Zhou A (2017) Compressive strength and microstructure of fly ash based geopolymer blended with silica fume under thermal cycle. Cem. Concr. Compos 78(2017):108
Preethi P, Sintha N, Raj MP, Tamilarasan K, Vinith R (2020) WITHDRAWN: exploration on geopolymer concrete using GGBS and silica fume
Puertas F, Palacios M, Manzano H, Dolado JS, Rico A, Rodríguez J (2011) A model for the C-A-S-H gel formed in alkali-activated slag cements. J Eur Ceram Soc 31(12):2043–2056
Rokita M, Handke M, Mozgawa W (2000) The AlPO4 polymorphs structure in the light of Raman and IR spectroscopy studies. J Mol Struct 555(1–3):351–356
Saad M, Abo-El-Enein SA, Hanna GB, Kotkata MF (1996) Effect of silica fume on the phase composition and microstructure of thermally treated concrete. Cem Concr Res 26(10):1479–1484
Sahnoun RD, Bouaziz J (2012) Sintering characteristics of kaolin in the presence of phosphoric acid binder. Ceram. Int. 38:1–7. https://doi.org/10.1016/j.ceramint.2011.06.058
Sellami M, Barre M, Toumi M (2019) Synthesis, thermal properties and electrical conductivity of phosphoric acid-based geopolymer with metakaolin. Appl Clay Sci 180:105192. https://doi.org/10.1016/j.clay.2019.105192
Senff L, Hotza D, Repette WL, Ferreira VM, Labrincha JA (2009) Influence of added nanosilica and/or silica fume on fresh and hardened properties of moratrs and cement pastes. Adv Appl Ceram 108:418–428. https://doi.org/10.1179/174367609X422108
Shaikh FUA, Supit SWM (2014) Mechanical and durability properties of high volume fly ash (HVFA) concrete containing calcium carbonate (CaCO3) nanoparticles. Constr Build Mater 70:309–321. https://doi.org/10.1016/j.conbuildmat.2014.07.099
Shaikh FU, Supit SW, Barbhuiya S (2017) Microstructure and nanoscaled characterization of HVFA cement paste containing nano-SiO_2 and nano-$CaCO_3$. J Mater Civ Eng 29(8):04017063
Singh B, Ishwarya G, Gupta M, Bhattacharyya SK (2015) Geopolymer concrete: a review of some recent developments. Constr Build Mater 85:78–90
Sivasakthi M, Jeyalakshmi R, Rajamane NP, Jose R (2018) Thermal and structural micro analysis of micro silica blended fly ash based geopolymer composites. J Non-Cryst Solids 499:117–130
Sorelli L, Constantinides G, Ulm FJ, Toutlemonde F (2008) The nano-mechanical signature of ultra high performance concrete by statistical nanoindentation techniques. Cem Concr Res 38(12):1447–1456
Stefanovsky SV, Stefanovsky OI, Kadyko MI (2016) FTIR and Raman spectroscopic study of sodium aluminophosphate and sodium aluminum-iron phosphate glasses containing uranium oxides. J Non-Cryst Solids 443:192–198
Tanwongwan W, Wongkitikun T, Onpecht K, Srilai S, Assabumrungrat S, Chollacoop N, Eiad-ua A (2020) Surface enhancement and structure formation of metakaolin from Thailand kaolin on the various calcination temperature. Materials Today: Proceedings 23:777–781
Tchakouté HK, Rüscher CH (2017) Mechanical and microstructural properties of metakaolin-based geopolymer cements from sodium waterglass and phosphoric acid solution as hardeners: a comparative study. Appl Clay Sci 140:81–87. https://doi.org/10.1016/j.clay.2017.02.002
Tchakouté HK, Rüscher CH, Kamseu E, Djobo JN, Leonelli C (2017) The influence of gibbsite in kaolin and the formation of berlinite on the properties of metakaolin-phosphate-based geopolymer cements. Mater Chem Phys 199:280–288
Vanitha N, Jeyalakshmi R (2023) Structural study of the effect of nano additives on the thermal properties of metakaolin phosphate geopolymer by MASNMR, XPS and SEM analysis. Inorg Chem Commun 153:110758

Vanitha N, Revathi T, Sivasakthi M, Jeyalakshmi R (2022) Microstructure properties of poly (phospho-siloxo) geopolymeric network with metakaolin as sole binder reinforced with n-SiO_2 and n-Al_2O_3. J Solid State Chem 312:123188

Velez K, Maximilien S, Damidot D, Fantozzi G, Sorrentino F (2001) Determination by nanoindentation of elastic modulus and hardness of pure constituents of Portland cement clinker. Cem Concr Res 31(4):555–561

Wang, Y-S., J-G. Dai, Z. Ding, W-T. Xu,Phosphate-based geopolymer: formation mechanism and thermal stability, (2017).Materials Letters, https://doi.org/10.1016/j.matlet.2017.01.022

Wang, Y.-S., Alrefaei, Y., & Dai, J.-G. (2019). Silico-aluminophosphate and alkali-aluminosilicate geopolymers: a comparative review. Frontiers in Materials, 6. https://doi.org/10.3389/fmats.2019.00106

Wongkeo W, Thongsanitgarn P, Ngamjarurojana A, Chaipanich A (2014) Compressive strength and chloride resistance of self-compacting concrete containing high level fly ash and silica fume. Mater Des 64:261–269

Zhang L, Zhang F, Liu M, Hu X (2017) Novel sustainable geopolymer based syntactic foams: an eco-friendly alternative to polymer based syntactic foams. Chem Eng J 313:74–82

Zribi M, Baklouti S (2021) Phosphate-based geopolymers: a critical review. Polym Bull. https://doi.org/10.1007/s00289-021-03829-0

Zribi M, Samet B, Baklouti S (2020) Mechanical, microstructural and structural investigation of phosphate-based geopolymers with respect to P/Al molar ratio. J Solid State Chem 281:121025. https://doi.org/10.1016/j.jssc.2019.121025

Zyganitidis I, Stefanidou M, Kalfagiannis N, Logothetidis S (2011) Nanomechanical characterization of cement-based pastes enriched with SiO_2 nanoparticles. Mater Sci Eng, B 176(19):1580–1584

Publisher's Note